Computation of turbulent flow in an IFRF quarl burner

Neil A. Kelson & D. L. Sean McElwain *CiSSaIM, QUT*
John Truelove *BHP Research, Newcastle*

Queensland University of Technology CiSSaIM
Technical Report 96/5 December 1996

Executive Summary: Computation of turbulent flow in an IFRF quarl burner

Overview

A computational model for isothermal axisymmetric turbulent flow in a quarl burner is set up using the CFD package FLUENT. Numerical solutions obtained from the model are compared with available experimental data. A standard $k-\epsilon$ model and RNG–based $k-\epsilon$ models are used to model the turbulence, with the objective of investigating whether implementation of any RNG modifications will lead to improved flow predictions at this level of closure.

A difficulty is that the flow considered here features a confined vortex breakdown which can be highly sensitive to flow behaviour both upstream and downstream of the breakdown zone. Special care is taken so that both grid–independent and domain–independent results can be reported. In particular, we attempt to quantify uncertainties due to unknown inlet conditions.

Model	ν_t	σ_k	σ_ϵ	C_μ	$C_{\epsilon 1}$	$C_{\epsilon 2}$
Std	$C_\mu k^2/\epsilon$	1.0	1.3	0.09	1.44	1.92
R1	$C_\mu k^2/\epsilon$	0.7179	0.7179	0.085	1.42	1.68

Findings

Main Finding: We find that a two–equation $k-\epsilon$ model, with modified constants predicted by RNG theory (referred to as model R1 in the Report, see also Table above), captures the experimentally observed forward flow region within the turbulent inner recirculating zone. This finding is in apparent contrast to previous studies, most of which have concluded that either algebraic or differential Reynolds stress modelling is needed to correctly predict the observed flow features.

Other Findings: A number of other observations with respect to the numerics, turbulence modelling and flow physics are made in the Report, and are given below in point form.

- The PL scheme responds very slowly to significant grid refinement, and its use is not recommended for the accurate computation of the flow setup considered here.

- The Quick discretisation scheme responds rapidly with grid refinement, to the extent that grid–independent solutions on computationally feasible grids can be obtained.

- If the computational outlet is positioned too close to the rear of the breakdown zone, the predicted axial dimensions of the IRZ can be significantly increased. However, the computed flow in the upstream section of the vortex breakdown is relatively insensitive to the location of the computational outlet plane. These observations appear to be more consistent with the view that breakdown is related to an axisymmetric form of boundary layer separation, rather than being a manifestation of the presence of subcritical flow states.

- The computed flow in the IRZ is relatively sensitive to changes in the mean flow inlet conditions. Great care in modelling upstream mean flow conditions must be exercised.

- The computed flow in the IRZ may or may not be influenced by upstream turbulence. In particular, we note the following.

  - If the approach flow turbulence levels are less than the turbulence levels that would be otherwise generated within the front region of the IRZ, then the computed flow within the recirculation zone is independent of upstream turbulence conditions.
  - If the approach flow turbulence levels are of the same magnitude or greater than the turbulence levels that would be otherwise generated within the front region of the IRZ, then the interaction between the IRZ and bounding shear layer is significantly stronger. In this case, turbulence levels within the recirculating zone are significantly enhanced by the higher levels within the shear layer, and significant changes in the velocity profiles are noted, consistent with these increases.

- The so–called *stagnation point anomaly* arising from the Boussinesq eddy viscosity hypothesis is noticable, if at all, when the levels of turbulence in the approach flow are sufficiently high so as to materially affect the mean flow properties in this region.

- The correct prediction of turbulence levels within the IRZ appears to be vital in order to capture the observed IRZ mean flow features. Thus, we observe that the standard $k-\epsilon$ model overpredicts turbulence energy in the forward flow region of the IRZ, and predicts a single–celled recirculating zone, in poor agreement with experiment. Model R1, by contrast, correctly captures both turbulence levels and mean flow details in the forward flow region of the recirculating zone.

- Model R1 not only best captures the the observed flow features, but also exhibits a tendency for unsteadiness in a localised region where an instability called the *precessing vortex core* is sometimes observed in swirl burners. This provides additional

indirect evidence that the flow physics is being adequately captured at this level of closure.

- To a first approximation, the model R1 results suggest that the eddy viscosity is approximately constant across the flow within the IRZ.
- The computed IRZ flow structure appears to be sensitive to relatively small changes in the predicted eddy viscosity.
- Modifications to the constant $C_{\epsilon 2}$, and to a lesser extent the turbulent Prandtl numbers σ_k and σ_ϵ, lead to the greatest changes in the predicted eddy viscosity levels.
- The standard wall function treatment returns acceptable wall values for the upstream mean velocities, but agreement is progressively worse downstream.
- Our results suggest that computed profiles far downstream are largely determined by the wall boundary conditions rather than the bulk flow turbulence modelling. This implies that improvements to the wall modelling should yield comparitively better results for flow in the downstream section of the recirculating zone (we have not tested this hypothesis).

Contents

Abstract

A computational model for isothermal axisymmetric turbulent flow in a quarl burner is set up using the CFD package FLUENT, and numerical solutions obtained from the model are compared with available experimental data. A standard $k-\epsilon$ model and and two versions of the RNG $k-\epsilon$ model are used to model the turbulence.

One of the aims of the computational study is to investigate whether the RNG based $k-\epsilon$ turbulence models are capable of yielding improved flow predictions compared with the standard $k-\epsilon$ turbulence model. A difficulty is that the flow considered here features a confined vortex breakdown which can be highly sensitive to flow behaviour both upstream and downstream of the breakdown zone. Nevertheless, the relatively simple confining geometry allows us to undertake a systematic study so that both grid–independent and domain–independent results can be reported. The systematic study includes a detailed investigation of the effects of upstream and downstream conditions on the predictions, in addition to grid refinement and other tests to ensure that numerical error is not significant.

Another important aim is to determine to what extent the turbulence model predictions can provide us with new insights into the physics of confined vortex breakdown flows. To this end, the computations are discussed in detail with reference to known vortex breakdown phenomena and existing theories.

A major conclusion is that one of the RNG $k-\epsilon$ models investigated here is able to correctly capture the complex forward flow region inside the recirculating breakdown zone. This apparently pathological result is in stark contrast to the findings of previous studies, most of which have concluded that either algebraic or differential Reynolds stress modelling is needed to correctly predict the observed flow features. Arguments are given as to why an isotropic eddy–viscosity turbulence model may well be able to capture the complex flow structure within the recirculating zone for this flow setup.

With regard to the flow physics, a major finding is that the results obtained here are more consistent with the view that confined vortex breakdown is a type of axisymmetric boundary layer separation, rather than a manifestation of a subcritical flow state.

Keywords: turbulence modelling, RNG, swirl, vortex breakdown, axisymmetric flow

Introduction

Vortex breakdown is a complex phenomena which can occur in fluid flows with moderate to high tangential or swirl velocity. In its axisymmetric form, breakdown is characterised by the presence of a primary localised region of recirculation or flow reversal downstream of a concentrated vortex core flow. An important industrial internal flow application is in connection with inner recirculation zones (IRZ) observed in swirl burners. In such devices it is important for the aerodynamics to be adequately understood as a precursor to successful modelling of the entire combustion process.

Axisymmetric vortex breakdown usually has a number of identifiable features. The upstream or approach flow is usually steady and consists of streamlines nearly parallel to the vortex axis. The approach flow may be either laminar or turbulent. At some location downstream the streamlines rapidly diverge and a recirculation zone or bubble begins to form. The structure of the recirculation zone can be complex and the dynamics is not fully understood. The upstream end of the bubble is often delineated by a front stagnation point, although axial flow through the centre of the breakdown zone can also occur. In addition, the bubble may be multi–cellular. Other possibilities include the formation of additional recirculation zones or a turbulent wake at the downstream end of the primary breakdown. In internal flow applications, the IRZ flow is typically highly coupled with that of the bulk flow, *i.e.* the presence of walls, blockages and other geometric features can introduce additional physical processes which may influence the final breakdown form. Also, the correct prediction of the internal structure of the vortex breakdown is usually of primary importance. This is especially true in combustion applications, where the breakdown region acts directly to affect flame shape, stability and other characteristics. The adequacy of the turbulence modelling can be subtly dependent on such flow conditions, and there is an ongoing need to provide detailed information on the performance of computational models via concrete examples [29].

The problem considered

The flow setup considered here corresponds to a test case of the International Flame Research Foundation (IFRF) for which experimental data is available for the mean and fluctuating axial and tangential velocities [13]. The flow data was obtained using a laser–Doppler velocimeter, and consists of transverse measurements across a number of downstream axial stations. The flow geometry is shown in Figure 1, and consists of an inlet pipe, a quarl section and a cylindrical furnace. The location of the burner cross sections where measurements were performed is also shown.

A key flow feature is that the ratio of the furnace to inlet pipe diameters is less than 3, so that the flow can be regarded as highly confined [33]. Also, the swirl was generated by a rotating honeycomb, so the initial vorticies had a solid–body rotation with a nearly uniform axial velocity profile across the inlet, and negligible radial velocity downstream from the generator. The problem considered is therefore an example of a highly confined, initially solid–body rotation

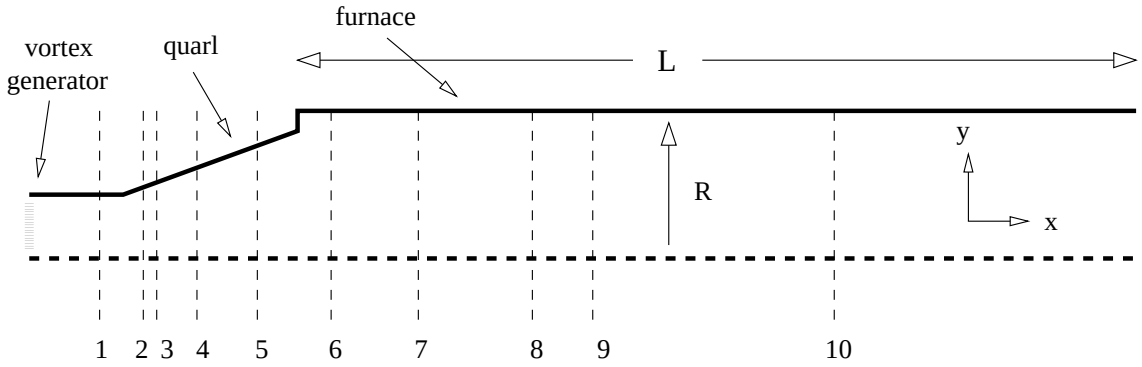

Figure 1: Schematic of the flow geometry. The inlet pipe is of length $140mm$ and radius $95mm$, the quarl is of length $260mm$ and maximum radius $190mm$, and the furnace is of length $5500mm$ and radius $220mm$. Locations of the transverse measurement stations are also shown. The first station is at $x = 105mm$.

flow. The latter is not only directly relevant to industrial flow applications, but also represents a demanding test for both computation and modelling. The difficulties arise primarily because the flow considered here features a confined vortex breakdown which can be highly sensitive to flow behaviour both upstream and downstream of the breakdown zone. In addition, the measurements indicate that the recirculating zone includes the presence of a forward flow region or inner cell structure. Such structures are sometimes observed, *e.g.* the early experiments of Faler & Leibovich [10], or the more recent DNS studies of Spall *et al.* [26], although a single–celled recirculating zone appears to be more common. In turbulent flow systems, in particular, only single–celled structures were observed in confined systems until the mid 1980's [31]. No definitive explanation appears to be available as to why a multi–cellular vortex breakdown zone should arise in preference to the simpler single–celled structure, although Faler & Leibovich propose that the action of fluctuations within the IRZ provides a possible mechanism, while Spall *et al.* speculate that the inclusion of viscous effects may be required to get the correct internal cell structure.

Review of earlier work

Previous work on confined turbulent vortex breakdown has mainly considered the performance of various turbulence models against given experimental data sets, in order to determine their strengths and weaknesses (*e.g.* [16, 17, 33, 1]). Important issues include the ability of the model to adequately predict the decay of mean swirl velocity and to capture the characteristics of the recirculation zone.

The reliability of studies which attempt definitive turbulence model evaluation exercises are dependent on issues such as numerical accuracy and choice of boundary and initial conditions being adequately addressed. While numerical accuracy is of generic concern in all CFD studies, for confined and strongly swirling flow with vortex breakdown, solutions can also be strongly dependent on inlet and outlet specifications. In such cases, a systematic investigation of the various aspects to the total computational model is indicated, but is usually considered too time consuming to be undertaken. This can make an accurate assessment of the evaluation exercise difficult. By way of illustration, we review existing studies due to Wanik & Schnell

[32], Benim [1], Weber *et al.* [33], and Choudhury [6], who have studied the flow setup being considered here.

In Wanik & Schnell's work [32], computed finite difference scheme solutions were obtained using a 27×23 grid, the $k-\epsilon$ model and hybrid differencing. In general, the results of Wanik & Schnell were in poor agreement with experiment: the predicted IRZ location begins too far upstream, the extent of recirculation within the IRZ is too strong, and the computed peak values of axial velocity at a number of cross–stream stations are significantly lower than the experimentally measured peak values. Previous experience with the $k-\epsilon$ turbulence model suggests that these results may be due to the highly diffusive nature of the $k-\epsilon$ model or the built–in assumption of an isotropic eddy–viscosity [25]. In Wanik & Schnell's work, however, it is more likely that excessive amounts of numerical (or false) diffusion were present due to the coarse grid and hybrid differencing scheme used. This false diffusion would lead to poor agreement with experiment in ways consistent with the shortcomings in their computed results noted above, irrespective of any shortcomings or otherwise in the turbulence modelling.

In Benim's paper [1], a finite element method was employed in conjunction with both a standard $k-\epsilon$ model and algebraic stress model (ASM) for the turbulence. A discontinuity–capturing streamline–upwind procedure for the convective terms was used in an effort to minimise numerical diffusion, and a 32×28 finite element grid was used. The likelihood of excessive numerical diffusion in Wanik & Schnell's work is also implied by the corresponding results obtained by Benim using a less diffusive convective discretisation scheme, which yielded significantly better agreement of $k-\epsilon$ model predictions with experiment. Benim also demonstrated that further agreement could be obtained by using an algebraic stress model instead of the $k-\epsilon$ model. However, neither model was found to satisfactorily capture the experimentally observed forward flow region within the IRZ.

The accuracy of the computed results of Benim are also open to question in the same manner as those of Wanik & Schnell's. Specifically, the level of numerical diffusion in Benim's computed results was not established conclusively because no grid refinement tests were performed. The absence of the latter seriously weaken Benim's arguments for numerical accuracy based on a comparison of results for two alternative convective discretisation schemes. In addition, the sensitivity or otherwise of Benim's computed solutions to changes in those inlet or boundary conditions which require modelling was not established. In our opinion, the uncertainty in model predictions due to changes in unknown inlet quantities needs to be established for swirling flow computations, as our own experience indicates that moderate changes in the inlet turbulence dissipation rate, for example, can significantly affect the downstream predictions for mean and turbulence quantities [18]. The importance of the inlet dissipation profile with reference to other work in swirling flows is discussed again later.

Weber *et al.* [33] have also presented finite volume computations for the present flow setup using $k-\epsilon$, algebraic and differential stress models. They used quadratic upstream differencing (Quick) for the convective terms, and the burner quarl was represented in the computations as a series of steps. They noted that increasing their mesh from 45×34 to 80×60 produced only small differences in the predicted axial and tangential velocities, which suggests that grid independent solutions had been obtained. Their results indicate that the algebraic and differential stress models yielded similar predictions, suggesting that the transport of Reynolds stresses played only a small role in determining the overall turbulence energy of the flow. Predictions obtained with the stress models were found to be in overall good agreement with experiment, although the strength of flow reversal within the IRZ was in general overpredicted. The computed $k-\epsilon$

predictions were in worse agreement with experiment. We note that Weber *et al.*'s turbulence energy inlet profile differed from Benim's. No sensitivity of results to changes in the inlet dissipation rate was investigated, and the mixing–length expression that was used also differs, by a factor of 1.4, from that used by Benim.

More recently, brief results for the present flow setup have also been presented by Choudhury and co–workers [6] (see also Boysan [5]). To model the turbulence, a Renormalization Group based $k-\epsilon$ model (RNG) was used, and differential Reynolds stress model (DSM) computations were also undertaken for model performance comparision purposes. A 26×209 grid was used in conjunction with the Quick convective discretisation scheme.

The results of Choudhury [6], which consist only of a presentation of mean streamlines and a comparison of mean axial velocity with experiment across one station, suggest that the RNG model can yield turbulent swirling flow predictions of comparable accuracy to that obtained by a DSM. In particular, the mean streamlines indicate that a forward flow region within the IRZ is captured by the RNG model. As with the studies reviewed above, the numerical accuracy of the results, and the sensitivity of the computed solutions to changes in upstream conditions, was not discussed.

Objectives

In this work, a computational study of turbulent swirling flow in the IFRF quarl burner is undertaken, and results are compared with available experimental data. The standard $k-\epsilon$ model and RNG based $k-\epsilon$ models are used to model the turbulence.

One of the aims of this study is to investigate whether RNG based $k-\epsilon$ turbulence models are capable of yielding improved flow predictions compared with the standard $k-\epsilon$ turbulence model. The relatively simple confining geometry allows us to realise this aim by undertaking a systematic study so that both grid–independent and domain–independent results can be reported. The systematic study includes a detailed investigation of the effects of upstream and downstream conditions on the predictions, in addition to grid refinement and other tests to ensure that numerical error is not significant. The results presented here appear to be of substantially higher quality than those reported in earlier work.

Another important aim is to determine to what extent the turbulence model predictions can provide us with new insights into the physics of confined vortex breakdown flows. To this end, the computations are discussed in detail with reference to known vortex breakdown phenomena and existing theories.

Mathematical model and numerical method

The Reynolds averaged equations for isodensity turbulent flow can be written in cartesian tensor notation as follows.

$$\frac{\partial U_i}{\partial x_i} = 0 \tag{1}$$

$$\frac{\partial U_i}{\partial t} + \frac{\partial}{\partial x_j}(U_i U_j) = \frac{-1}{\rho}\frac{\partial P}{\partial x_i} + \frac{\partial}{\partial x_j}\left[\nu_0\left(\frac{\partial U_i}{\partial x_j} + \frac{\partial U_j}{\partial x_i}\right) + \overline{u_i u_j}\right]. \tag{2}$$

In the above, U_i and P are the time averaged mean velocity and mean pressure, while $\overline{u_i u_j}$ is the Reynolds stress tensor. The Reynolds stresses represent new, unknown terms which require modelling.

Two–equation $k-\epsilon$ Modelling

In the two–equation $k-\epsilon$ framework, the Boussinesq hypothesis (see *e.g.* [25]) is used to replace the Reynolds stresses via the introduction of an eddy viscosity, ν_{eddy}. The task of modelling is to then provide a prescription for the eddy viscosity over the entire flow domain. To this end, ν_{eddy} is described in terms of the turbulent kinetic energy, k, and dissipation rate, ϵ. These are in turn obtained via the solution of partial differential equations. Thus,

$$\frac{\partial k}{\partial t} + \frac{\partial}{\partial x_i}(U_i k) = \frac{\partial}{\partial x_i}(\frac{\nu_t}{\sigma_k}\frac{\partial k}{\partial x_i}) + \nu_t S^2 - \epsilon \tag{3}$$

$$\frac{\partial \epsilon}{\partial t} + \frac{\partial}{\partial x_i}(U_i \epsilon) = \frac{\partial}{\partial x_i}(\frac{\nu_t}{\sigma_\epsilon}\frac{\partial \epsilon}{\partial x_i}) + C_{1\epsilon}\frac{\epsilon}{k}\nu_t S^2 - C_{2\epsilon}\frac{\epsilon^2}{k} - R \ , \tag{4}$$

where S_{ij}, the rate of strain, and S^2 are given by

$$S_{ij} = \frac{1}{2}\left(\frac{\partial U_i}{\partial x_j} + \frac{\partial U_j}{\partial x_i}\right), \qquad S^2 = 2S_{ij}S_{ij} \ . \tag{5}$$

In the standard $k-\epsilon$ model (denoted STD), ν_{eddy} is prescribed via

$$\nu_{eddy} = \nu_0 + \nu_t \ , \ \nu_t = C_\mu \frac{k^2}{\epsilon} \ , \tag{6}$$

the term R in Equation (4) is set to zero, and the empirical constants are set to $C_\mu = 0.09$, $\sigma_k = 1.0$, $\sigma_\epsilon = 1.3$, $C_{1\epsilon} = 1.44$, and $C_{2\epsilon} = 1.92$.

The RNG theory has been successful in developing turbulence models which are similar to the Std model. For high Reynolds numbers (Re), equations identical in form to Equations (3) and (4) are obtained, and the values of the model constants are theoretically determined. The theory can also provide extended prescriptions for the model constants, eddy viscosity, and turbulence transport equations. For example, the theory predicts [34] that $\sigma_k = \sigma_\epsilon = 1/\alpha$, where α is a function of ν_{eddy}, namely,

$$\left|\frac{\alpha - 1.3929}{\alpha_0 - 1.3929}\right|^{0.6321} \left|\frac{\alpha + 2.3929}{\alpha_0 + 2.3929}\right|^{0.3679} = \frac{\nu_0}{\nu_{eddy}} \ , \ \alpha_0 = 1 \ . \tag{7}$$

In the high Re limit, Equation (7) predicts the value of $\alpha = 1.3929$, or $\sigma_k = \sigma_\epsilon = 0.7179$.

Recent extensions [35] have aimed to extend the applicability of the ϵ–equation to accommodate high strain rates via the derivation of an additional term, R, namely

$$R = \frac{C_\mu \eta^3 (1 - \eta/\eta_0)}{1 + \beta\eta^3}\frac{\epsilon^2}{k} \ , \ \eta = \frac{Sk}{\epsilon} \ , \ \eta_0 = 4.38 \ , \ \beta = 0.012 \tag{8}$$

The present study considers turbulent vortex breakdown predictions obtained using successive RNG modifications to Std model, as given in Table 1. Thus, R1 denotes a $k-\epsilon$ model where only the high Re values of the model constants, as derived in [36], are implemented. For model R2, Equation (7) and (8) are also included.

Table 1: Two–equation turbulence models used in this study

Model	ν_t	σ_k	σ_ϵ	C_μ	$C_{\epsilon 1}$	$C_{\epsilon 2}$	R
Std	Eqn (6)	1.0	1.3	0.09	1.44	1.92	0
R1	Eqn (6)	0.7179	0.7179	0.085	1.42	1.68	0
R2	Eqn (6)	Eqn (7)	Eqn (7)	0.085	1.42	1.68	Eqn (8)

Inlet conditions

For the $k-\epsilon$ model computations, inlet profiles of axial, radial and tangential velocities, turbulence energy and turbulence dissipation rate are required. Here we position the computational inlet to coincide with the first measurement station downstream of the swirl generator.

For the mean velocities, two different sets of profiles across the computational inlet plane are used. The first set of profiles are based directly on the measurements for the mean axial and tangential velocities at the first station. The second specification uses averaged profiles which assume that a solid–body rotational flow prevails at the computational inlet. Thus, for the second set the inlet conditions are approximated by a flow with uniform axial velocity of $4.7ms^{-1}$, and Swirl number of 0.7, corresponding to a peak tangential velocity of $6.58ms^{-1}$. In both cases the inlet radial velocity is assumed to be zero. The two sets of profiles are shown in Figure 2.

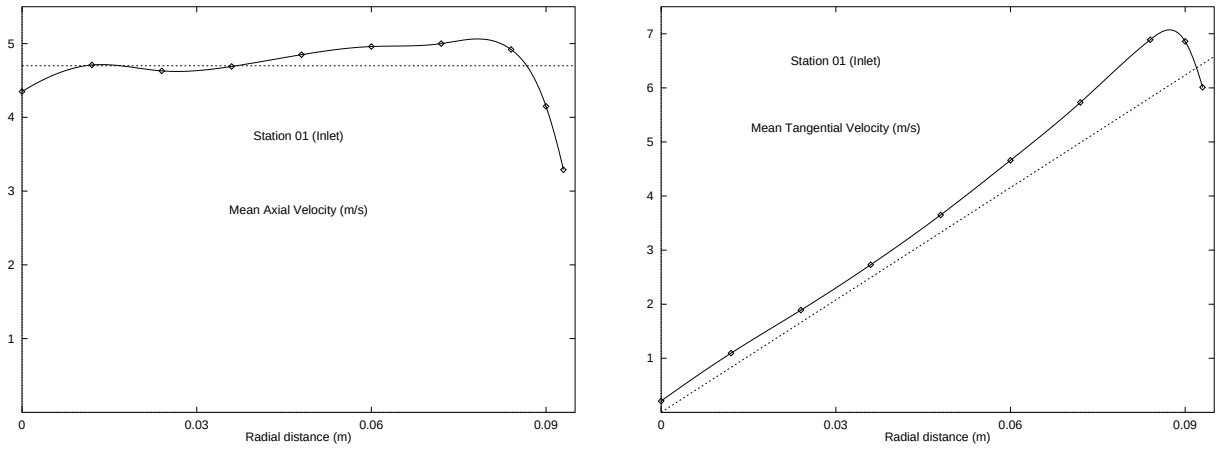

(a) Axial velocity at Stn 1 (b) Tangential velocity at Stn 1

Figure 2: Inlet mean velocity profiles (Stn 1): IC1 (expt) $-\diamond-$; IC2 (solid–body: $U_0 = 4.7m/s$ & $W_0 = y \times 6.58m/s$) $--$.

For the turbulence energy across the inlet, modelling is needed because the normal stresses were not all measured. Two methods are used here. For the first method, the inlet turbulence energy is estimated from the measured profiles of the mean square axial and tangential velocity fluctuation profiles, by first estimating the mean square radial velocity fluctuation profile via

$$\overline{v^2} = \left(\overline{u^2} + \overline{w^2}\right)/2 \tag{9}$$

Using this method to estimate the inlet turbulence energy yields an almost uniform distribution, with a sharp peak near the inlet pipe wall, as shown in Figure 3(b). This way of specifying the

inlet conditions for k was the one used by Benim [1]. Alternatively, a uniform inlet turbulence energy profile can be obtained via the ratio of the turbulence energy to the inlet mean axial velocity, *i.e.*

$$I = \frac{\overline{u^2} + \overline{v^2} + \overline{w^2}}{2{U_0}^2} = \frac{k}{{U_0}^2} \tag{10}$$

Weber *et al.* [33] used this second method with $I = 0.01$, which in fact overpredicts, by up to 2.5 times, the inlet turbulence energy estimated by the first method for over 80% of the inlet pipe radius. Interestingly, the fluctuating velocities obtained by Weber *et al.* at Station 4 using the $k-\epsilon$ model are overpredicted by a similar amount, so it is not clear whether a poor choice of inlet conditions has lead to this overprediction or whether it is due to the shortcomings of the $k-\epsilon$ model. A study of the sensitivity of downstream turbulence to changes in inlet turbulence levels is undertaken here to resolve this question. The two different inlet turbulence energy profiles are compared in Figure 3(b), along with the $I = 0.05$ specification, also used by Weber *et al.*.

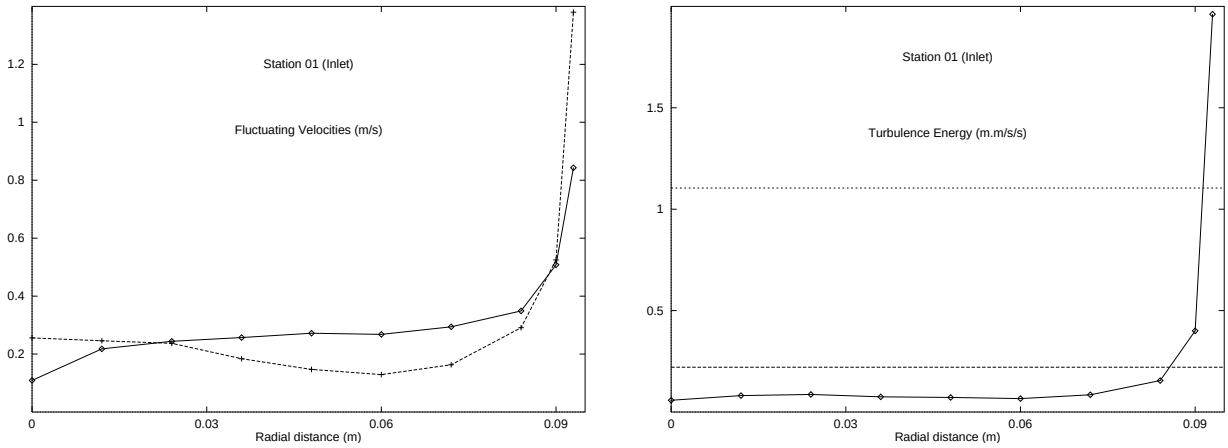

(a) Fluctuating velocities at Stn 1 (b) Turbulence energy at Stn 1

Figure 3: Inlet turbulence profiles (Stn 1): (a) axial velocity (expt) $-\diamond-$ & tangential velocity (expt) $-+-$; (b) Turbulence energy IC1/IC2 $-\diamond-$; IC3 $--$; IC4 $\cdots$.

Modelling is required for the inlet conditions for the turbulence dissipation, as no measurements of this quantity were made. Here, the unknown inlet turbulence dissipation rate is estimated from the measured inlet turbulence energy using the expression

$$\epsilon = \delta_\epsilon \left(\frac{C_\mu^{\frac{3}{4}} k^{\frac{3}{2}}}{0.01 R_i} \right) \ , \tag{11}$$

where R_i is the radius of the inlet pipe, and δ_ϵ is a constant. It is important to note the modelling assumptions implicit in this expression. Firstly, Equation (11) is based on an equilibrium or mixing–length assumption, where production and dissipation of turbulence are assumed to balance (*i.e.* transport and history effects are assumed negligible). Secondly, a single characteristic length scale l_m of the turbulence is assumed (*i.e.* $\epsilon \sim k^{3/2}/l_m$), and is usually taken equal to about 1–5% of the inlet diameter. Different values of δ_ϵ correspond to different estimates for the characteristic length scale of the turbulence near the inlet. For example, Benim used $\delta_\epsilon = 1$ (about 3% of the inlet diameter), while Weber *et al.* chose $\delta_\epsilon = 1.43$. On the other hand, the studies by Hogg & Leschziner [16], and more recently Sharif & Wong [24], found after some

Table 2: Inlet conditions

	—— Variable ——				
Inlet Cond.	U	V	W	k	ϵ
IC1	Expt data	0	Expt data	Expt data & Eqn 9	Eqn 11, $\delta_\epsilon = 1.0$
IC2	Uniform	0	Solid–Body	Expt data & Eqn 9	Eqn 11, $\delta_\epsilon = 1.0$
IC3	Uniform	0	Solid–Body	Eqn 10 ($I = 0.01$)	Eqn 11, $\delta_\epsilon = 1.0$
IC4	Uniform	0	Solid–Body	Eqn 10 ($I = 0.05$)	Eqn 11, $\delta_\epsilon = 1.0$
IC5	Uniform	0	Solid–Body	Eqn 10 ($I = 0.05$)	Eqn 11, $\delta_\epsilon = 0.5$
IC6	Uniform	0	Solid–Body	Eqn 10 ($I = 0.05$)	Eqn 11, $\delta_\epsilon = 0.1$

optimisation that a turbulent length scale of around 18% of the inlet diameter, or $\delta_\epsilon \sim 0.16$, was needed to obtain the best results.

In this study we treat δ_ϵ as a free parameter. In support of a parametric study of solution dependence on changes in the inlet dissipation rate as just proposed, we cite, in addition to the works previously mentioned, the study of confined swirling flow due to Nikjooy & Mongia [21]. In their study, three different prescriptions for ϵ_{inlet} were used. Overall, the major differences between the three inlet dissipation profiles appeared in the peak and centreline regions. On comparing predictions obtained with the different profiles, they found that the calculated mean flow field showed somewhat different behaviour, the predicted reverse flow regions, in particular, being affected. With regard to turbulence quantities, the effects of ϵ_{inlet} on shear stress were found to be serious near the inlet where, in their flow setup, the IRZ was formed, and a wide disparity in the predicted turbulent normal stresses was also noted. The importance of inlet boundary conditions has also been argued by other authors. (See, for example, Leschziner & Rodi [20], or more recently Dong & Lilley [8].) In light of these studies, it would seem necessary that the effect of inlet dissipation profiles on predictions need to be determined for turbulent swirling flows.

The different inlet conditions used in this study are summarised in Table 2.

It is of interest to speculate as to why turbulent vortex breakdown flows appear to be comparitively sensitive to upstream conditions. A possible explanation arises on consideration of the nearly cylindrical approach flow. From laminar flow theory, it is known that a concentrated vortex core flow can act as a "fluid amplifier", in the sense that changes in the outer flow can lead to relatively larger changes in the vortex core interior [14]. While corresponding mechanisms for turbulent flow have not, to our knowledge, been discussed, a plausible reason for sensitivity to upstream changes in the dissipation rate profile would be that it directly affects the upstream turbulence energy and eddy–viscosity levels, which in turn affect the upstream mean flow in the pre–breakdown concentrated vortex core flow. These changes are then amplified in the mean vortex core flow in essentially the same way as would occur in laminar flow. The amplified changes in the upstream mean vortex core flow would then be expected to produce significant differences in the downstream mean flow in the breakdown region. Essentially, what is suggested here is that the upstream turbulence levels affect the upstream mean flow, which then affects the mean flow in the breakdown zone.

An alternative proposal would be that the upstream turbulence levels affect the downstream turbulence activity within and around the breakdown region, this in turn affecting the mean flow within the IRZ. A possible way to differentiate between the two mechanisms is as follows.

A pipe flow is considered where the inlet is far enough away from the breakdown region for the turbulence activity at the inlet to have decayed. If, however, the downstream IRZ is still affected by changes in turbulence activity at the inlet, then it is clear that the only mechanism is through the changes that the inlet turbulence profiles have had on the mean vortex core flow upstream of the breakdown.

Our use of different inlet turbulence profiles allows us to comment on both of the proposals just given in the light of results obtained for the present flow setup. As discussed later, we shall argue that turbulence activity within the breakdown region is nearly independent of relatively low turbulence levels in the approach flow. However, low approach flow turbulence levels do appear to determine turbulence levels in the upstream region of the bounding shear layer via convective transport. On the other hand, relatively high turbulence levels in the approach flow are found to enhance turbulence activity within the IRZ, and the mean flow is affected, both upstream and within the recirculating zone.

Discretisation and solution procedure

The governing Reynolds–averaged Navier–Stokes equations for axisymmetic, incompressible flow are solved in conjunction with the turbulence transport equations, utilising the CFD code FLUENT. The discretised equations are obtained using the control volume method of Patankar [22], and a segregated approach is used for each transport equation in conjunction with the SIMPLEC algorithm of van Doormaal & Raithby [30] to resolve the pressure–velocity coupling. For improved efficiency, the multigrid method is used to solve the resulting pressure–correction equation, while alternating direction Line Gauss Seidel is used for the discretised mean momentum and turbulence transport equations. The total flow solver algorithm is a well–tested, reliable and reasonably efficient approach, and the code has been subjected to extensive benchmarking to ensure numerical accuracy [7].

The computational domain is a cross section of the axisymmetric IFRF burner which consists of the inlet pipe, quarl and furnace sections, from the furnace axis (or symmetry line) to an outer wall. The furnace length was initially set at $L = 4m$.

The radial grid lines are distributed uniformly in the inlet pipe and furnace sections, where the pipe generators are parallel to the symmetry axis. Initially, the grid is constructed with 19 and 22 interior cells in the inlet pipe and furnace section, respectively. In the quarl section, 20 radial grid lines are equally spaced from the pipe axis to the wetted side of the quarl wall, again leading to 19 interior cells in the radial direction. The resultant cell skewness in the quarl is less than 20^o from orthogonal, and can be expected to provide a better prescription than a straircase cell modelling of the quarl wall for quantities such as the wall shear stress.

In the axial direction, uniform grid spacing in each of the three sections of the computational domain is used, because strong coupling between all regions of the flow can be expected in a vortex breakdown type flow, so that careful resolution of the flow over the entire computational domain may be necessary. For the initial axial grid line distribution on the coarsest grid considered here, 2 cells (of width $17.5mm$) are used in the inlet pipe, and axial cell widths of $20mm$ are used in the other sections. For a $4m$ furnace length, the number of interior cells is 2×19 in the inlet pipe, 13×19 in the quarl, and 200×22 in the furnace. The coarse grid (217×24 grid lines in total) therefore consists of approximately evenly spaced cells with low skewness and mesh expansion ratios over the entire domain, with cell aspect ratios in the range

of 2 to 4.

The coarsest grid used in this work is shown in Figure 4. For the grid refinement studies, the axial grid spacing is successively halved.

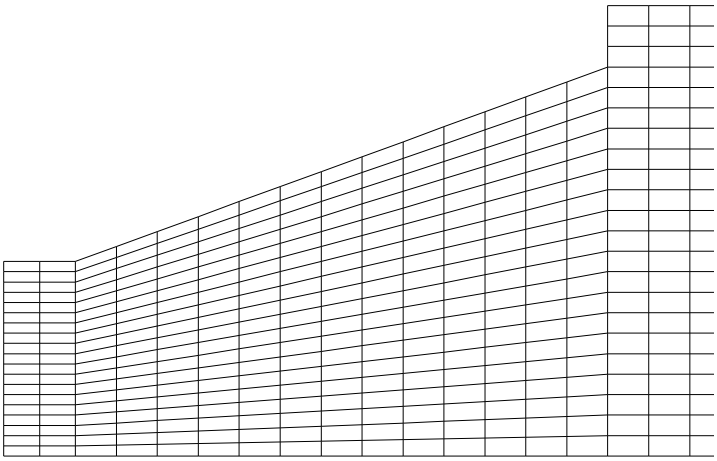

Figure 4: Details of the coarsest grid used in this study.

In order to establish conditions under which domain–independent and grid–independent solutions can be obtained, sample computations with Power Law (PL) convective differencing, Second Order Upwind Differencing (Soud) and Quick schemes are made on different length furnaces using successively refined grids. To establish iterative convergence, a number of global iterations are performed until the maximum residual sum of the solution arrays indicates that a final steady state has been obtained. A number of points throughout the computational domain are also monitored as an additional check that transients have decayed. As the discrete equations tend to be stiffer when the higher order Soud and Quick schemes are used, a good initial guess in the form of a converged PL solution is used to improve the route to convergence for these schemes. For the latter, small oscillations of less than 1% around steady state values would often persist in the solution arrays. In addition to the increased stiffness, these are also attributed to the fact that the higher order schemes are implemented as deferred corrections in the code (which often leads to weak numerical oscillations on the approach to steady state [23]), rather than being an indication of any small underlying instability in the actual flow.

Results and discussion

Model Std

Sensitivity to outlet Conditions

According to the theory of Benjamin [2, 3, 4], vortex breakdown is due to the presence of subcritical flow somewhere within the flow domain. For the present flow setup, the observed inner recirculation may be due in part to vortex breakdown, and this raises the possibility that flow downstream of the breakdown may be subcritical. Subcritical outflow conditions will

allow information, in the form of travelling waves, to travel upstream from the exit plane to all of the subcritical flow domain, potentially changing it via the formation of standing wave patterns. In such cases, special treatment of the outlet boundary conditions may be required. We note that in this flow setup, there was no end contraction in the experimental rig, but there was a 90^o bend located $5.5m$ downstream from the quarl. At the $4m$ cross–section, no fluid was experimentally observed to be re-entering the flow domain. Thus, we assume that the flow is supercritical across this plane, and a computational outlet with the usual zero–gradient conditions for all variables is imposed on a furnace of initial length $L = 4m$. We stress that flow supercriticality across the exit plane is, in effect, a modelling assumption only, since the fact that the flow is observed to be entirely downstream at this station in no way actually guarantees it.

In order to investigate whether the length of the computational domain could be reduced (thereby reducing computing times and facilitating further grid refinement), we decided to test if the location of the outlet plane would materially affect the upstream predictions. To this end, computed solutions using the $k - \epsilon$ model and furnace lengths of $L = 4m$, $3m$, $2m$, $1.5m$, $1m$ and $0.5m$ were obtained on 217×24, 167×24, 117×24, 92×24, 67×24 and 42×24 grids, respectively. The grids for the shorter length furnaces are constructed in the same manner as the 217×24 grid described earlier, so that the corresponding control volumes in each of the grids are identical. In addition to the location of the outlet, the effect of different convective differencing schemes is also investigated. Table 3 summarises key differences in the computed solutions.

Table 3: Std model/IC2 solution characteristics as a function of furnace length L. For a description of variables see the text.

Scheme	L (m)	ψ_{min} (m^2/s)	ψ_{max} (m^2/s)	U_{min} (m/s)	U_{max} (m/s)	x_{front} (mm)	x_{back} (mm)	k_{max} (m^2/s^2)	$(\nu_t)_{max}$ (kg/ms)
PL	0.5	-.0040340	.022157	-.90788	5.4255	121.97	709.70	1.9000	.019423
	1.0	-.0039206	.022163	-.87004	5.4256	121.88	614.96	1.8740	.019030
	1.5	-.0038939	.022165	-.86520	5.4256	121.90	610.03	1.8727	.019041
	2.0	-.0039029	.022164	-.86723	5.4256	121.90	611.18	1.8735	.019045
	3.0	-.0038969	.022165	-.86609	5.4256	121.90	610.38	1.8732	.019047
	4.0	-.0038945	.022165	-.86539	5.4256	121.90	610.03	1.8728	.019043
Soud	0.5	-.0057712	.022676	-.98536	5.4930	118.56	> 795	2.0207	.017951
	1.0	-.0056283	.022702	-.91088	5.4933	118.44	682.01	1.9868	.017627
	1.5	-.0056340	.022702	-.90947	5.4932	118.44	680.41	1.9861	.017625
	2.0	-.0056251	.022702	-.90941	5.4934	118.44	680.36	1.9861	.017624
	3.0	-.0056252	.022702	-.90941	5.4932	118.44	680.35	1.9861	.017624
	4.0	-.0056251	.022702	-.90942	5.4932	118.44	680.36	1.9861	.017625
Quick	1.0	-.0059584	.021839	-.87375	5.3392	119.96	705.72	2.0831	.017302
	1.5	-.0059655	.021836	-.87293	5.3393	119.95	704.74	2.0748	.017278
	2.0	-.0059780	.021835	-.87453	5.3393	119.93	706.08	2.0704	.017245
	3.0	-.0059950	.021838	-.87775	5.3393	119.92	705.51	2.0828	.017238
	4.0	-.0059815	.021837	-.87578	5.3394	119.92	705.81	2.0757	.017249

From Table 3, it is clear that for a given discretisation scheme, the location of the exit plane has very little effect on the solution parameters listed in Table 3 for computational domain lengths corresponding to furnace lengths of $1m$ or more. However, significant differences do appear on the shortest $795mm$ domain, corresponding to $L = 0.5m$. Most noticably affected is

the computed location of the back stagnation point, x_{back}, of the IRZ, defined as the point on the symmetry line where the mean velocity is zero. When the PL scheme is used, the effect of placing the exit plane at $x = 795mm$ (*i.e.* too close to the rear of the IRZ where the flow is not yet sufficiently fully developed) is to increase the computed axial dimensions of the recirculating zone by more than 20%. The computed solution using the Soud scheme shows a similar trend. In this case, however, inflow near the symmetry line of the exit plane is predicted. This can be interpreted to mean that the predicted axial dimensions of the IRZ has increased to such an extent that the location of the back stagnation point now lies outside the computational domain. The computed solution, however, is no longer strictly valid, since the computed exit flow does not behave in a way which is physically consistent with the zero gradient boundary conditions applied at the exit plane. Thus, any conclusions drawn from this particular computed solution must be treated with caution. In light of these observations, further computations using this very short computational domain were abandoned. In particular, a solution using the Quick scheme was not attempted.

To further investigate the predictions, a detailed graphical analysis was undertaken. To begin with, at each of the transverse measurement stations, the computed profiles of the mean axial velocity, mean tangential velocity and turbulence energy as obtained on the different length domains were separately compared. For a given choice of discretisation scheme (either PL, Soud or Quick) no differences in the respective profiles could be seen to graphical accuracy[1] for furnace lengths of $1m$ or more. As an additional check, a random comparison of solution array values indicated differences of less than 1% in cell values (*i.e.* the estimated maximum error due to the convergence criterion) for the $1.5m$, $2m$, $3m$ and $4m$ grid results. However, a similar scrutiny of the solution arrays for the $1m$ furnace revealed that the computed solution on this length domain differed by up to approximately 7% for the axial velocity, and less than 4% for both the tangential velocity and turbulence energy, when compared with solutions computed on the longer domains. In general, the larger differences were observed to occur where the cell values being compared were small in magnitude.

We can conclude from the above observations that the exit plane may be located as close as $1m$ from the quarl without significantly affecting the predicted upstream flow, irrespective of whether the actual exit flow is subcritical or not. Subsequent computations are therefore performed with the computational outlet initially located conservatively at $1.5m$ downstream from the quarl.

As a final point, we wish to address the question of whether the close proximity of the exit plane to the rear of the IRZ has a predominantly local effect on the flow behaviour or not. To this end, a closer scutiny of the computed solutions on the very short $L = 0.5m$ computational domain was undertaken. The significance of the question may be appreciated by recalling that in the explainatory theory due to Benjamin, vortex breakdown is due to standing wave patterns arising in regions of subcritical flow. Now if Benjamin's theory is essentially correct, it would follow that any changes in exit flow conditions in the vicinity of the IRZ should have a significant impact on the entire flow behaviour in the recirculating zone, since the nature of the upstream–travelling waves in the subcritical region would be directly altered, and these in turn would lead to a correspondingly altered final standing wave breakdown flow pattern.

With the preceeding remarks in mind, a graphical analysis was again undertaken, with com-

[1] Two plots are here considered identical to graphical accuracy if absolute differences are everywhere smaller than can be detected easily by eye. For a $55mm \times 75mm$ XY plot, differences smaller than 1 part in 250 of full scale can easily be detected by inspection.

puted profiles of the axial velocity, tangential velocity and turbulence energy obtained on the $L = 0.5m$ length domain being separately compared at each of the transverse measurement stations with the corresponding $1.5m$ results. In Figure 5, differences which arise in the computed mean velocity profiles at Stations 8 and 9 (using Soud) due to the alternative placements of the exit plane are shown (Station 10 results cannot be compared as this axial station lies outside the computational domain of the $0.5m$ furnace geometry). The results presented in Figure 5 are entirely representative of the greatest differences that can noticed in the computations using the Soud scheme. Upstream, the differences become progressively smaller to the extent that for Stations 2 through to 6 inclusive, no differences in the mean velocity profiles obtained on the two different length domains can be observed. Differences which arise when using the PL scheme were found to be even less than those noticed in the Soud results.

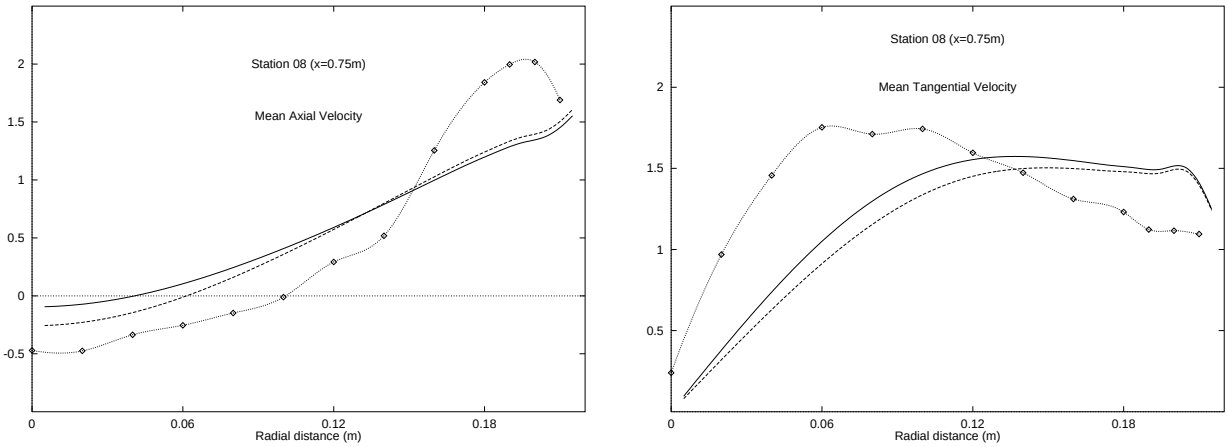

(a) Axial velocity at Stn 8

(b) Tangential velocity at Stn 8

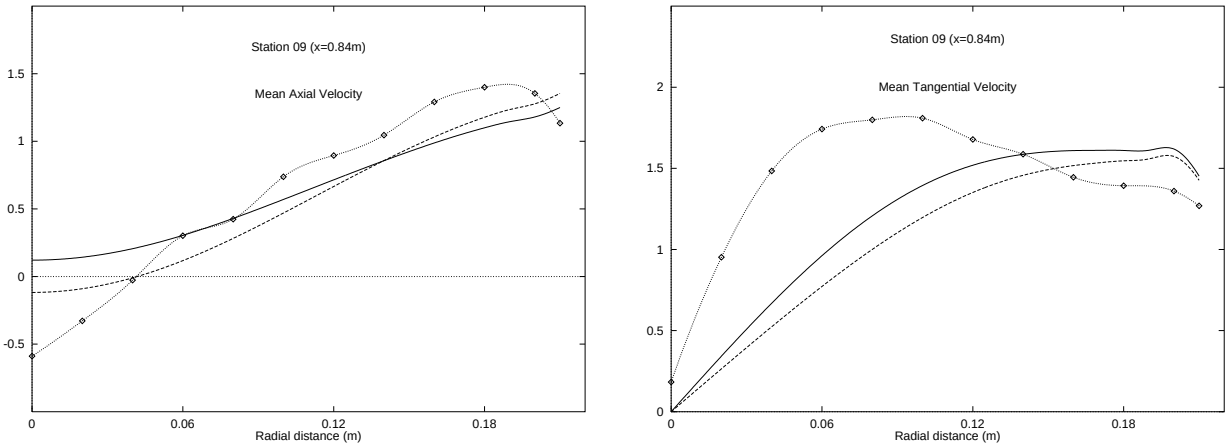

(c) Axial velocity at Stn 9

(d) Tangential velocity at Stn 9

Figure 5: Std Model/IC2/Soud velocity profiles at Stns 8 & 9: $1.5m$ — ; $0.5m$ - - ; Expt $-\diamond-$.

Given that Stations 4 through to 9 all traverse the IRZ (with Station 6 traversing near the IRZ centre), and the fact that for the Soud calculations the exit plane can be viewed as being actually located, in part, within the central recirculating zone, we conclude from the above observations that the downstream exit conditions affect the IRZ flow conditions local to the exit plane only. The evidence presented here would therefore not seem to provide any definite computational support for Benjamin's theory of vortex breakdown in this case, as any weak effect of the exit conditions on the upstream flow within the IRZ would seem to be more reasonably attributed to its recirculating nature. Rather, our results obtained with the Std model would seem to be more consistent with the view that breakdown is related to the concept of an axisymmetric

form of boundary layer separation, as originally proposed by Gartshore, Hall and others (see Hall [15]).

For an alternative view, it is of interest to mention here the results of Hogg & Leschziner [16], who computed a swirling flow with a central non–swirling jet. The flow rate of the jet was sufficiently strong for no central recirculation zone to be observed in the measurements. In their computations, an alternative outlet flow condition in the form of an explicitly prescribed axial velocity profile across the outlet was considered, in addition to the usual situation where zero gradient conditions are applied. While such an approach is not useful from a practical point of view, it did allow them to investigate the effect of exit conditions on their turbulence model predictions. Indeed, the effect of the different exit conditions on their $k-\epsilon$ model results for the centreline axial velocity indicate, as found here, that differences were largest near the exit and diminish upstream. Away from the symmetry axis, however, their computed profiles showed little differences. Hogg & Leschziner make the assumption that the flow is in fact subcritical in the sense of Benjamin's theory only in a small region close to the symmetry axis (in spite of the absence of any flow reversal, which they attribute to the presence of the central jet), and conclude that the $k-\epsilon$ model fails to capture the subcritical nature of the flow. Clearly, a similar conclusion could be drawn from the Soud results presented here, provided, of course, that the flow considered here is assumed to be in a subcritical state over a region containing the recirculating zone. For a like conclusion to be drawn from the PL scheme results, where the back stagnation point is located inside the computational domain, at least some cross section of the flow which continues downstream from the IRZ to the exit plane would also have to be considered as subcritical.

Numerical accuracy

In order to establish the conditions for which computed results would be free of significant numerical error, grid refinement tests employing the PL, Soud and Quick schemes were performed.

For the grid refinement tests we decided to initially fix the number and location of the radially placed grid lines. This ensures that the numerical implementation of the inlet, wall and symmetry conditions remains unchanged, *i.e.* the coupling between the bulk flow, inlet and wall modelling is "frozen" at the discrete level. By increasing the density of the axially placed grid lines only, the numerical uncertainty in the bulk flow prediction can therefore be assessed in isolation. The upwind implementation of the zero–gradient outlet condition will, however, be affected if the axial width of the cells contiguous to the exit plane is reduced, but we do not expect this to impact on the flow predictions, in light of the results presented in the previous section. For the grid refinement tests, the Std model with the IC2 inlet condition on the $L = 1.5m$ domain was computed on 92×24, 182×24 and 362×24 grids. The finer grids were constructed by successively halving the axial grid line separation.

Key features of the computed solutions on the refined grids are given in Table 4. Quantities given are cell values only, with the exception of the locations of the front and back stagnation points. The latter were estimated from the axial velocity cell values on the symmetry axis via straightforward linear interpolation.

From Table 4, the key quantities listed for the PL scheme either increase or decrease monotonically with grid refinement. This is not unexpected, and would appear to reflect the fact

Table 4: Std model/IC2/$L = 1.5m$ solution characteristics as a function of grid refinement and discretisation scheme.

Scheme	Grid	ψ_{min} (m^2/s)	ψ_{max} (m^2/s)	U_{min} (m/s)	U_{max} (m/s)	x_{front} (mm)	x_{back} (mm)	k_{max} (m^2/s^2)	$(\nu_t)_{max}$ (kg/ms)
PL	092×24	-.0038939	.022165	-.86520	5.4256	121.90	610.03	1.8727	.019041
	182×24	-.0044375	.022799	-.90409	5.5248	116.30	619.92	2.1181	.019175
	362×24	-.0048512	.023341	-.94136	5.5992	114.03	630.84	2.2279	.019179
Soud	092×24	-.0056340	.022702	-.90947	5.4932	118.44	680.41	1.9861	.017625
	182×24	-.0061108	.022873	-.87240	5.6017	116.50	704.50	1.9985	.016903
	362×24	-.0058490	.023298	-.81389	5.6472	117.86	694.79	1.9404	.016505
Quick	092×24	-.0059655	.021836	-.87293	5.3393	119.95	704.74	2.0748	.017278
	182×24	-.0066920	.022716	-.96735	5.4868	119.68	738.52	2.1472	.017925
	362×24	-.0063147	.021907	-.98923	5.8075	120.42	738.21	1.8728	.019043

that for recirculating 3D flows, this scheme is little more than first–order accurate and entirely numerically diffusive. For the Soud and Quick schemes, however, monotonic behaviour is not clearly evident. This may be due to the fact that pointwise rather than interpolated extreme values have been tabulated, but is more likely to be due to the leading order error terms in the higher order schemes being both numerically diffusive and dispersive in nature [11]. The reduction in the sum of these two sources of numerical error would be expected to behave in a non–linear way with grid refinement. As a final observation on the tabulated values, we note that for two key indicators of the IRZ properties, namely ψ_{min} and x_{back}, the Soud and Quick scheme predictions are in reasonable agreement with each other, and significantly different from the PL scheme results obtained on any of the grids considered.

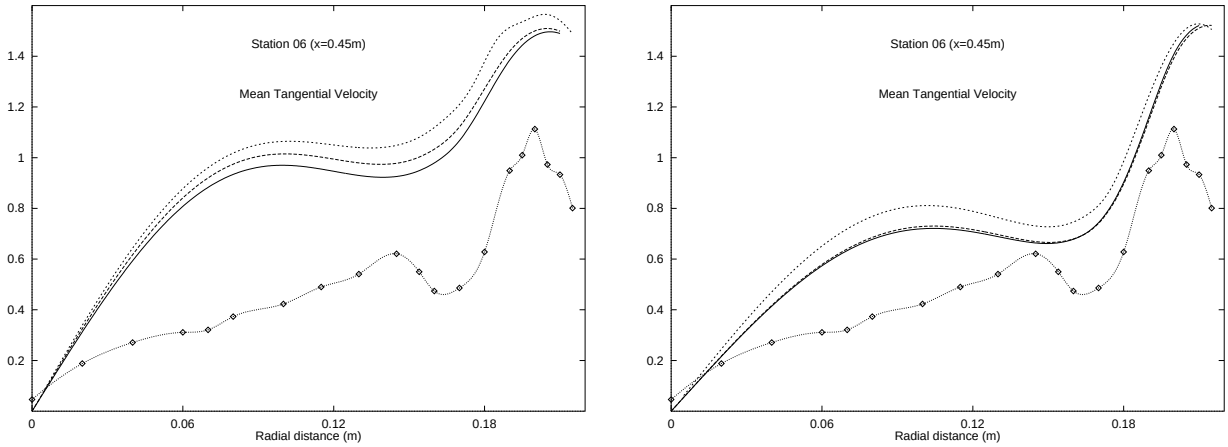

(a) Tangential velocity at Stn 6 (PL) (b) Tangential velocity at Stn 6 (Quick)

Figure 6: Std model/IC2 profiles at Stn 6 on 362×24 (—), 182×24 (– –) and 92×24 ($\cdots$) grids, with Expt ($- \diamond -$): (a) PL; (b) Quick.

The rate of spatial convergence of the different discretisation schemes is brought into sharper focus in Figure 6, where results for the tangential velocity at Station 6 using the Std model with inlet condition IC2 are presented. In Figure 6(a), results with the PL scheme show differences of less than 10% in the predicted profiles for successive grid refinements, and it could be tentatively concluded that further grid refinement would not lead to further significant

reductions in discretisation error. In this manner, and in the absence of further numerical tests, a (false) sense of numerical accuracy using this scheme could be gained.

An entirely different picture emerges by comparison of Figure 6(a) with Figure 6(b), which presents results for the Quick scheme. In Figure 6(b) we see that the Quick scheme responds rapidly with grid refinement to produce virtually co–incident profiles using either the 182×24 or 362×24 grid. This rapid spatial convergence of the Quick scheme observed in the profiles presented in Figure 6(b) is completely representative of the solution behaviour at all stations, as is demonstrated by an additional presentation of profiles for this case, given in Figure 7. We conclude that the 182×24 grid in conjunction with the Quick scheme is sufficiently fine to yield essentially grid independent results for the $L = 1.5m$ furnace, and this grid line density will be used in subsequent computations.

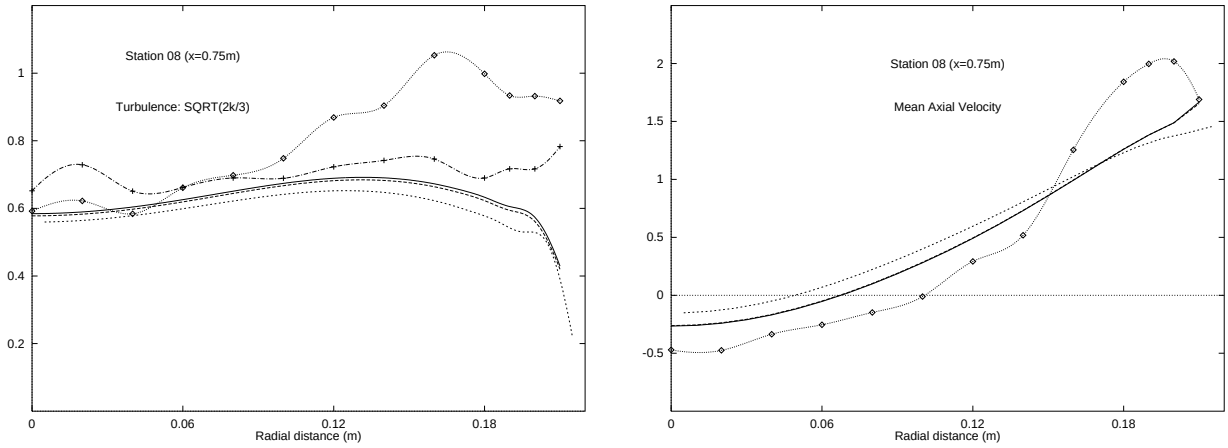

(a) Turbulence at Stn 8 (b) Axial velocity at Stn 8

Figure 7: Std model/IC2/Quick profiles at Stn 8 on 362×24 (—), 182×24 (– –) and 92×24 $(\cdots)$ grids: (a) $\sqrt{2k/3}$ with Expt (u' $-\diamond-$, w' $-+-$); (b) Axial velocity with Expt ($-\diamond-$).

Returning to Figure 6(a), we note that unacceptably large differences between the PL and Quick predictions persist, even with significant grid refinement. In light of the observations just made, we can conclude that the PL scheme responds very slowly to significant grid refinement, at the same time retaining significant numerical error. While in principle it should be possible to reduce false diffusion and other numerical errors to negligibly low levels, the use of the PL scheme to obtain grid–independent predictions for this flow setup would appear to require an excessively large number of grid points.

In Figure 8, turbulence profiles obtained via the PL, Soud and Quick schemes at Stations 3 and 4 are compared with experiment. Results presented are again for the Std model/IC2/$L = 1.5m$ on 182×24 grid. In Figure 8(a), the PL, Soud and Quick schemes at Stations 3 are essentially identical to graphical accuracy. This can be attributed to the the fact that the local mean flow is not greatly skewed with respect to the computational grid, this evidently having a beneficial effect via the reduction of errors due to numerical diffusion. Indeed, for Stations 2 and 3, both of which are located upstream of the front stagnation point in the almost parallel approach flow region, differences in the mean axial and tangential velocities due to choice of discretisation scheme were also not observed to be large.

In Figure 8(b), turbulence quantities at Station 4 are compared. This station is located just downstream of the front stagnation point, and traverses the upstream region of highly recir-

culating flow within the IRZ. Here, the PL scheme leads to up to 50% numerical error in the plotted profile of $\sqrt{2k/3}$ (*i.e.* up to 100% error in the computed quantity k), when compared with the grid–independent Quick result. Furthermore, the numerical error is in the wrong direction, resulting in an even greater overprediction when compared with the measurements. On the other hand, the Soud profile, while not free of numerical error, is in good quantitative agreement with the Quick profile. These observations are representative of results at subsequent downstream stations, namely, all profiles obtained using the Soud scheme are similar to the Quick scheme results obtained on the same grid, while the PL distributions are in general noticably different.

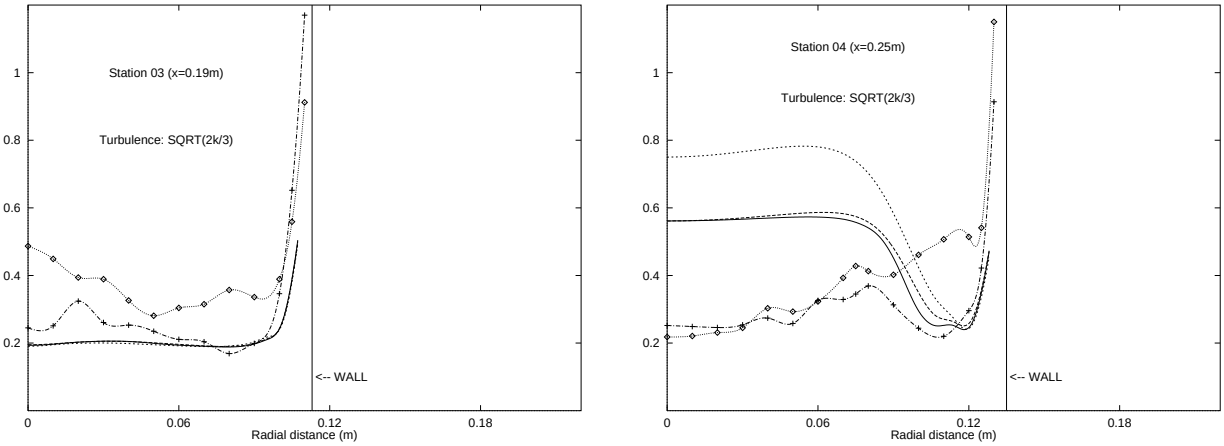

(a) Turbulence at Stn 3 (b) Turbulence at Stn 4

Figure 8: Std model/IC2/182 × 24 grid profiles at Stns 3 & 4 with Quick (—), Soud (– –) and PL ($\cdots$) schemes *c.f.* Expt ($u' - \diamond -$, $w' - + -$): (a) $\sqrt{2k/3}$ at Stn 3; (b) $\sqrt{2k/3}$ at Stn 4.

Figure 8(b) also underlines certain key points for the correct computation and modelling of swirling flow involving vortex breakdown–induced recirculating zones, some of which have been noted by other authors. Firstly, it is quite clear in the light of the large differences in Figure 8(b), that accurate convective differencing schemes *must* be used for the turbulence transport equations as well as the mean transport equations, if grid–independent results on computationally feasible grids are to be obtained. This is particularly true of flow *within* the recirculating zone, where differences due to choice of discretisation are more pronounced. As results for models R1 and R2 will later show, the correct prediction of turbulence levels within the IRZ appears to be vital in order to capture the observed mean flow features. It follows that overprediction of turbulence energy within the IRZ, whether due to inadequate turbulence modelling or numerical diffusion, will lead to a single–celled recirculating zone, in poor agreement with experiment.

The above finding is in contrast to the view that the turbulent transport equations are often believed to be largely source term dominated, *i.e.* largely determined by local production and dissipation rates rather than convective transport, so that higher order convective differencing for these equations may not be required for accurate results (*e.g.* Leschziner & Rodi [19], Fu *et al.* [12]). With this in mind, and referring to Figure 8(b), we note that the $\sqrt{2k/3}$ profiles obtained with the different convective schemes begin to coincide in the vicinity of the wall. This may indicate that turbulent convective transport is indeed of less importance in the bounding shear layer. However, the near matching of the profiles may also simply reflect the fact that the flow–to–grid skewness is also low in the vicinity of the wall, reducing numerical diffusion.

Another idea frequently argued in the literature (*e.g.* Leschziner & Rodi [19]) is that the characteristics of the recirculation zone is greatly affected by diffusive transport in the bordering shear layer. Here, however, we have already noted that the correct prediction of turbulence quantities within the IRZ appears to be the key ingredient in order to capture the observed mean flow features. Further arguments for this point of view will be presented later in greater detail.

Sensitivity to inlet conditions

In practical applications, detailed measurements of the upstream flow produced by vane swirlers and other devices is often not available, and must be modelled. Unfortunately, for strongly swirling flow, the overall flow predictions can be rather sensitive to the details of the inlet conditions. To assess the extent of this sensitivity in the present flow setup, results are computed using the Quick scheme on 182×24 grid for the Std model using inlet conditions IC1 and IC2. The two inlet conditions are equivalent in the sense that the inlet plane mass flow rate and Swirl numbers are identical, and the turbulence profiles are unchanged.

The computed profiles are shown in Figures 9 and 10 along with the experimental results. In general, the profiles obtained using the two different inlet conditions yield noticably different results. For the approach flow (Stations 2 and 3) the use of condition IC1 leads to computed profiles which are in better agreement with the measured ones. In particular, the mean axial velocity at these two stations is significantly affected by the choice of inlet profiles, while the mean tangential velocity is less affected. The opposite is true of the profiles at Stations 4, 5, 6, and 7, all of which lie well within the computed recirculation zone. For these stations, the differences between the computed mean axial velocity profiles remain clearly noticible but are nevertheless significantly smaller, while the differences in the computed mean tangential velocity profiles are more pronounced.

In general, the differences in the computed profiles of Figures 9 and 10 are not so large that a suitably qualified assessment of the Std model's performance compared with experiment cannot be undertaken. However, before undertaking this assessment we decided to investigate the effect of upstream turbulence levels on the computed profiles. To this end, additional computations using inlet conditions IC3, IC4, IC5 and IC6 were undertaken.

The effect of the different inlet conditions on the mean velocity profiles is shown in Figure 11, while the effect on downstream turbulence levels is illustrated in Figure 12. With reference to Figure 12, we see that condition IC2 corresponds to the lowest levels of turbulence activity in the approach flow (Stations 2 and 3, Figures 12(a) and (b)), while condition IC6 corresponds to significantly higher levels. Inlet conditions IC4, IC5 and IC6 correspond to a fixed level of turbulence energy of $1.105 m^2/s^2$ across the inlet. These three inlet conditions prescribe successively lower inlet dissipation rate profiles (*i.e.* successively lower values of δ_ϵ), this leading to slower rates of turbulence energy decay from the inlet to Station 2. For condition IC6, for example, the turbulence energy is convected essentially without change between these two stations, while for conditions IC5 and IC4, energy levels have decayed by approximately 55% and 75%, respectively.

Referring again to Figure 12, we see that between Stations 2 and 3 the turbulence energy of the approach flow continues to decay slightly while being convected downstream, for all inlet conditions except IC6. Interestingly, it is in this axial interval that the flow approaches the

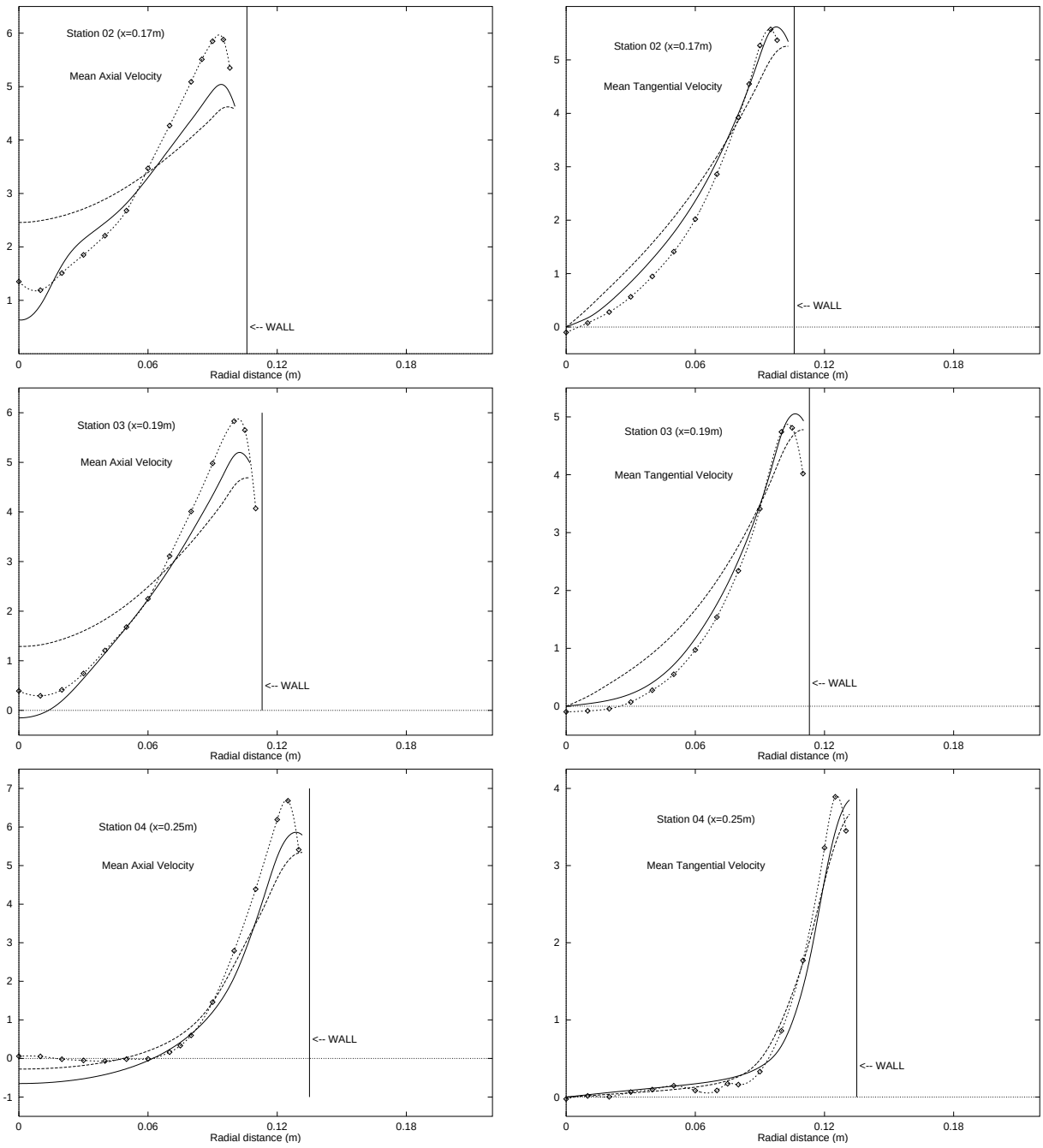

(a) Axial velocity (b) Tangential velocity

Figure 9: Comparison of Std model/Quick/182×24 grid/$L = 1.5m$ results using IC1 (—) & IC2 (– –) inlet conditions at Stations 2, 3 & 4 with Expt ($- \diamond -$).

front stagnation point and the streamlines diverge strongly. It is in this very flow region that the so–called stagnation point anomaly of the $k - \epsilon$ turbulence model should be in evidence, as very recently discussed, for example, by Durbin [9]. This "anomaly" refers to a deficiency in the constituitive Boussinesq eddy-viscosity relation, which can lead to the significant overprediction of turbulence energy as a stagnation point is approached. The problems arising from this anomaly are believed to be not so much associated with the flow in the vicinity of the stagnation point, where the flow is governed primarily by changes in the mean pressure. Rather, the excess turbulence energy produced is expected to be convected further downstream into the bounding shear layer, erroneously adding to the turbulence transport there. This in turn would be

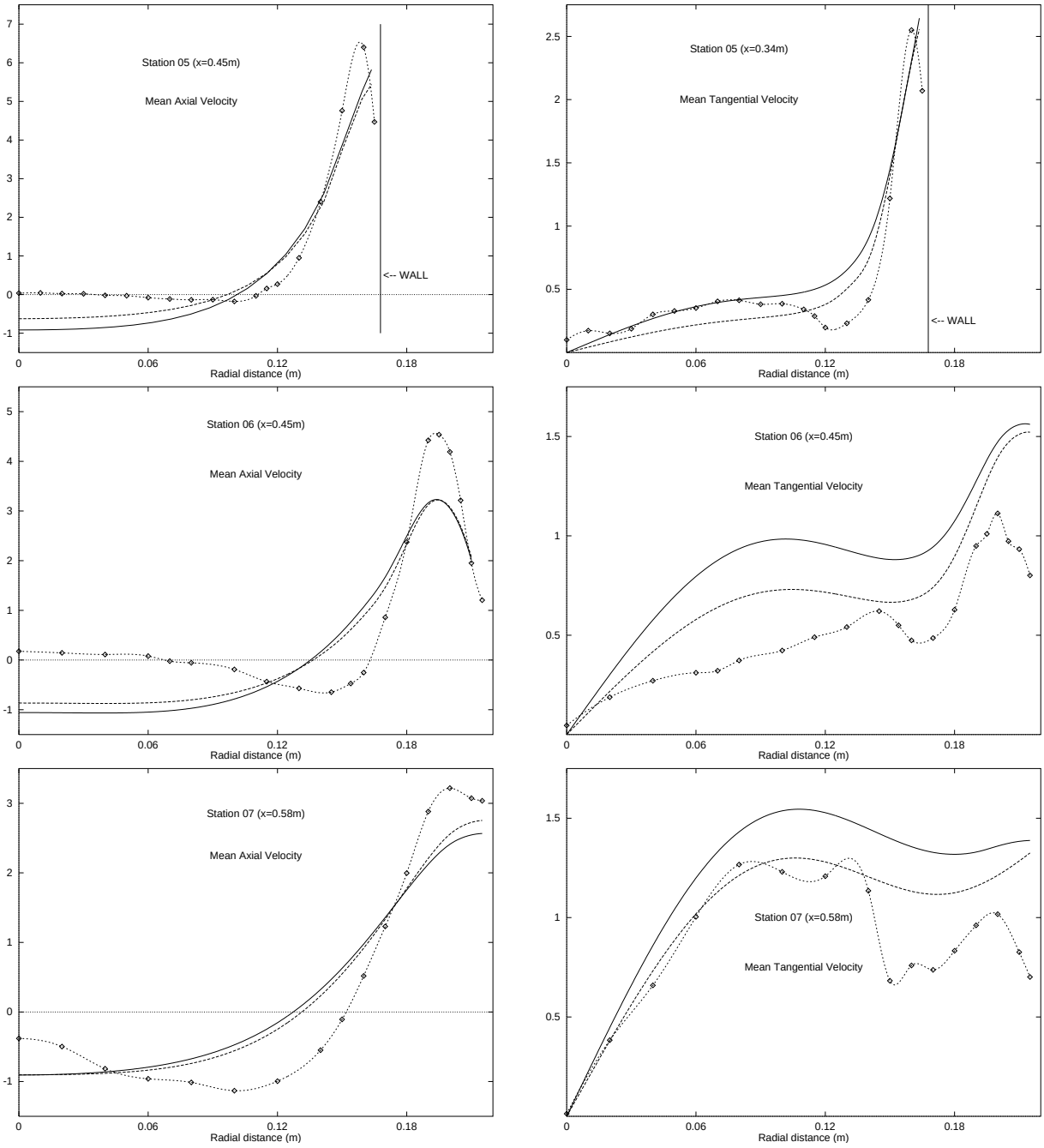

(a) Axial velocity (b) Tangential velocity

Figure 10: Comparison of Std model/Quick/182×24 grid/$L = 1.5m$ results using IC1 (—) & IC2 (– –) inlet conditions at Stations 5, 6 & 7 with Expt (– ◇ –).

expected to materially affect the properties of the enclosed recirculation zone.

The present results indicate that no evidence of the stagnation point anomaly can be found for inlet conditions IC3, IC4 or IC5. Furthermore, the mean axial and tangential velocity profiles in the approach flow region are unaffected by the different levels of free stream turbulence in the approach flow which is introduced by these different inlet specifications, as illustrated by the results presented in Figure 11 for Station 3. For inlet condition IC6, however, the upstream mean velocity profiles are now affected by the associated increase in turbulence levels in the approach flow. In addition, this is accompanied by an approximately 40% rise in the

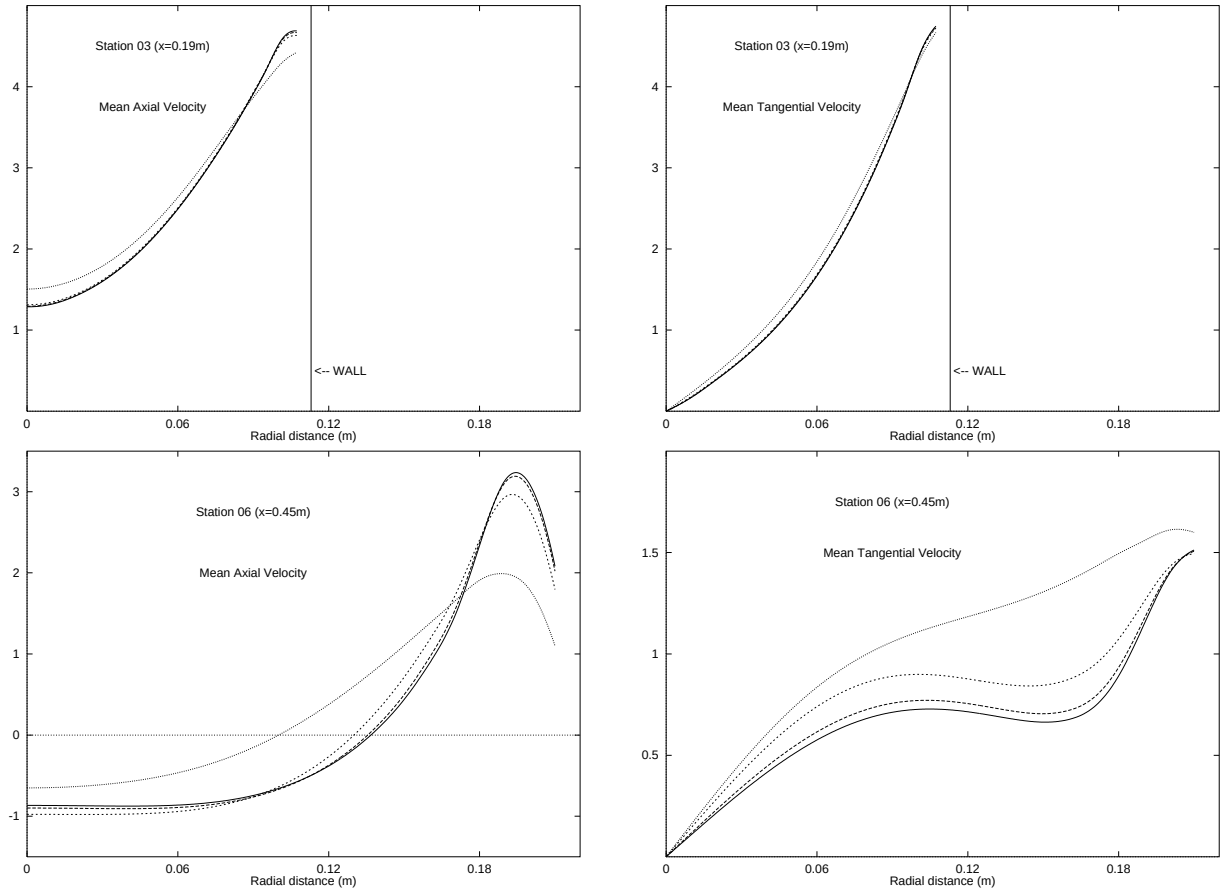

(a) Axial velocity (b) Tangential velocity

Figure 11: Comparison of Std model/Quick/182×24 grid/$L = 1.5m$ mean velocity profiles at Stations 3 & 6 using IC3 (—), IC4 (– –), IC5 (- - -) & IC6 ($\cdots$) inlet conditions.

turbulence energy between Stations 2 and 3. To determine if the rise is anomalous would require comparison of results with measurements corresponding to the higher inlet turbulence levels. Thus, the preceeding observations suggest that the stagnation point anomaly is noticable, if at all, when the levels of turbulence in the approach flow are sufficiently high so as to materially affect the mean flow properties in this region.

The effect of changes in the inlet turbulence conditions on the mean flow downstream is also given in Figure 11, where mean velocity profiles at Station 6 are presented. (The mean profiles at this station for inlet condition IC2 are not plotted because they are coincident with the IC3 results.) The profiles given are representative of the fact that only small differences in the mean profiles arise if condition IC4 is used instead of either condition IC2 or IC3. However, clearly noticable changes in the mean profiles result if IC5 or IC6 inlet conditions are used. In this case, the increased turbulence levels in the approach flow leads to a deterioration of the downstream predictions when compared with the measured profiles given earlier. Further information in the form of key solution characteristics for the different inlet conditions is given in Table 5. The tabulated results show, in particular, that the axial dimensions of the computed recirculating zone is reduced by increases in the approach flow turbulence levels by as much as 44% for the IC6 case.

As a final comment on the effect of upstream turbulence levels, we observe from Figure 12 that at Station 4 (see Figure 12(c)), the turbulence energy generated within the IRZ for conditions

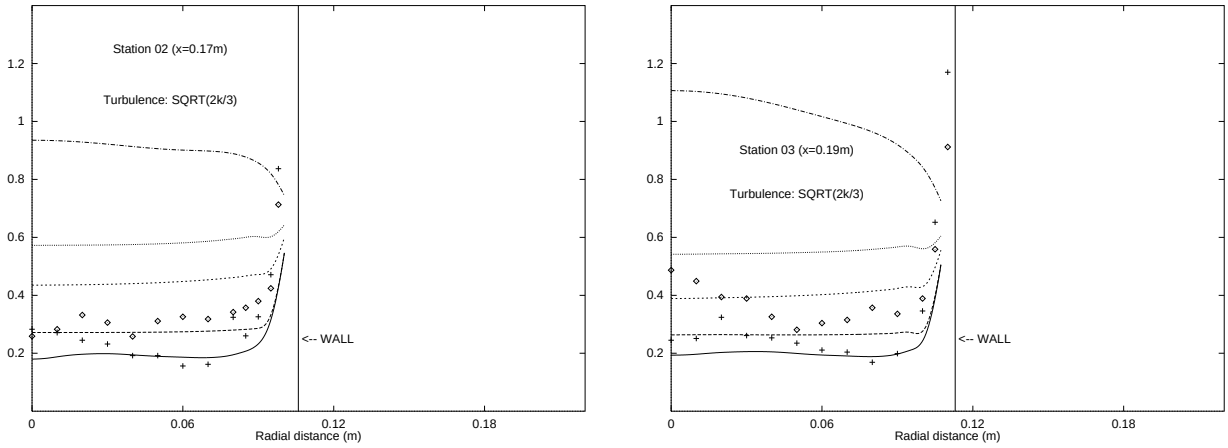

(a) Turbulence at Stn 2

(b) Turbulence at Stn 3

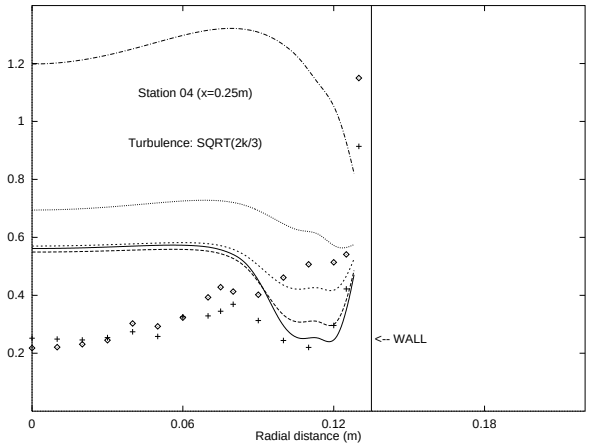

(c) Turbulence at Stn 4

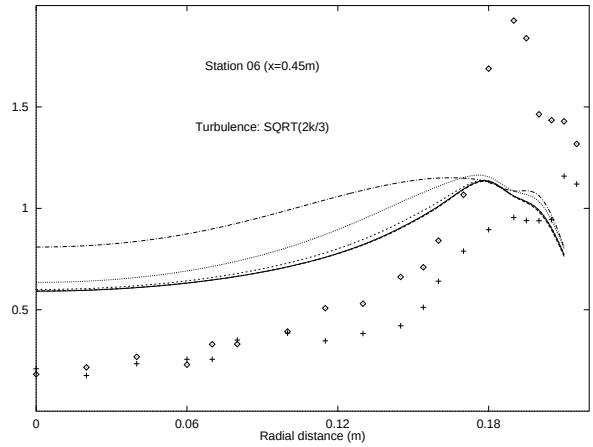

(d) Turbulence at Stn 6

Figure 12: Comparison of Std model/Quick/182×24 grid/$L = 1.5m$ $\sqrt{2k/3}$ turbulence profiles at Stations 2, 3, 4 & 6 using IC2 (—), IC3 (– –), IC4 (- - -), IC5 ($\cdots$) & IC6 ($-\cdot-$) inlet conditions, with Expt (u $\diamond$, w $+$).

Table 5: Std model/182×24 grid/$L = 1.5m$ solution characteristics as a function of inlet turbulence profiles.

Inlet	ψ_{min} (m^2/s)	ψ_{max} (m^2/s)	U_{min} (m/s)	U_{max} (m/s)	x_{front} (mm)	x_{back} (mm)	k_{max} (m^2/s^2)	$(\nu_t)_{max}$ (kg/ms)
IC2	-.0066920	.022716	-.96735	5.4868	119.68	738.52	2.1472	.017925
IC3	-.0067537	.022712	-.97354	5.4878	119.57	740.95	2.1266	.017972
IC4	-.0066229	.022717	-.97132	5.4809	119.23	729.14	2.1482	.018085
IC5	-.0057802	.022725	-.98007	5.4698	118.72	675.01	2.3522	.018853
IC6	-.0021922	.022500	-1.0783	5.4092	123.02	470.88	3.0906	.028322

IC2, IC3 or IC4 is nearly independent of their upstream levels at the previous Stations, all of which are clearly less by comparison. As a possible generalisation of this observation, we conclude that provided the energy levels in the approach flow in the immediate vicinity of the front stagnation point are clearly less than the turbulence energy levels that would be generated within the upstream region of the IRZ, then the mean flow predictions within the IRZ will be nearly independent of the approach flow turbulence levels.

A careful examination of the results for conditions IC2, IC3 and IC4 does, however, suggest a weak mechanism by which low turbulence levels in the approach flow can affect the downstream profiles. Comparison of the turbulence profiles at Stations 3 and 4 in Figures 12(b) and (c) indicate that although the turbulence levels within the IRZ at Station 4 are nearly independent of the corresponding levels at Station 3, the levels within the bounding shear layer at Station 4 (*i.e.* approx. $y > 0.1m$) are essentially those at Station 3 which have been convected without decay between the two stations. Subsequently, the IRZ and the shear layer interact via diffusion, turbulent momentum exchange, *etc.*, so that by Station 6, no differences in the bounding shear layer turbulence levels remain, while the turbulence levels within the IRZ at this station are slightly modified to the extent that the level corresponding to condition IC4 is just noticably higher than the IC2 and IC3 cases. This small rise in turn leads to a small but noticable change in the mean velocity profiles for case IC4 compared with cases IC2 and IC3 at Station 6, see Figure 11.

For conditions IC5 and IC6, the approach flow turbulence levels are of the same magnitude or greater than the turbulence levels that would be otherwise generated within the front region of the IRZ. We suggest that in these two cases, the interaction between the IRZ and bounding shear layer is significantly stronger, to the extent that turbulence levels within the recirculating zone are significantly enhanced by the higher levels within the shear layer. The significant changes in the mean axial and tangential velocity profiles at Station 6 shown in Figure 11 are consistent with these increases.

Sensitivity to wall conditions

In addition to the above computations, we also obtained sample solutions on a 182×48 grid. The new grid is constructed from the 182×24 grid by halving the radial grid spacing, and the Std model on $L = 1.5m$ geometry is again used. The IC1 inlet conditions are employed on both grids, this leading to small differences in the mass flow rate, Swirl number and turbulence levels at the discrete level across the inlet plane, due primarily to the assignment of inlet cell values in the sharp near–wall boundary layers in the measured profiles of Figures 2 and 3. The main point of interest here, however, is that the new radial spacing will in fact materially affect the discrete implementation of both the axisymmetry and, more importantly, the wall boundary conditions. Nevertheless, results for the new grid are found to yield graphically identical profiles to the 182×24 grid results, except in the immediate vicinity of the wall, where dimensionless distances obtained from the wall boundary conditions are essentially halved, *i.e.* now in the range $y^+ \sim 40 \rightarrow 50$. The results again support the conclusion that the Quick computations on the 182×24 grid yields grid independent results for this case, and also indicate that the results are not dependent on the dimensionless wall distance in the log–law boundary implementation, provided $y^+ > 40$.

Comparison with experiment

The various computations described above allow us to make a more informed assessment of the Std $k - \epsilon$ model performance against experimental results. We again focus on the results presented earlier in Figures 9 and 10, in particular the profiles at Stations 4, 5 and 6 which map out the experimentally observed forward flow region of the IRZ.

In general, the results presented here are in broad agreement with those presented earlier by

Benim [1] and Weber *et al.* [33], in the sense that no forward flow region in the recirculation zone is predicted. At Station 4 of Figure 9, for example, the peak of the computed mean axial velocity using either IC1 or IC2 inlet conditions is slightly low, while the extent of flow reversal near the symmetry axis is too great. This shortcoming is also evident in the mean axial velocity profiles at all subsequently plotted stations. Since the differences in the axial velocity profiles computed with either IC1 or IC2 conditions are not large at Stations 4, 5, 6 or 7, we cannot argue that these shortcomings are primarily due to misrepresentations in the inlet plane mean velocity profiles. Similarly, our investigations with different inlet turbulence profiles presented earlier indicate that any potential misrepresentation of upstream turbulence specifications is also unlikely to be responsible for shortcomings in the downstream axial velocity profiles, provided that turbulence energy in the approach flow is not too large (as is the case here). On the other hand, less firm conclusions would be obtained by examining instead the mean tangential velocity predictions with experiment, as the computed profiles tend to be more sensitive to changes in mean velocity profiles across the inlet plane. In the absence of firm error estimates on the experimental data, it is difficult to say with certainty that the tangential velocity prediction at Station 5 using inlet condition IC2, for example, lies within the experimental range (see Figure 10). The predicted profile at Station 6 using inlet condition IC1 does, however, appear to return swirl levels which are clearly too high when compared with experiment, supporting the conclusions previously reached via an examination of the mean axial velocity results.

While the results presented here indicate deficiencies in the Std $k-\epsilon$ model that have been observed in earlier studies, these shortcomings are significantly less pronounced. The corresponding computations due to Benim, for example, show noticably worse peak axial velocities than those obtained here. We argue that the source of this discrepency is the presence of numerical diffusion due to Benim's course grid calculations. The likely mechanism for error is that the numerical diffusion leads to greater turbulence energy levels in the upstream region of the IRZ (as illustrated in Figure 8), which in turn results in significantly lower peak axial velocities downstream (as illustrated in Figure 11), although this could not be verified because no turbulence results were given in Benim's work. In the case of Weber *et al.*'s results, the computed velocity profiles within the forward flow section of the IRZ are also significantly worse than those obtained here. For example, the mean axial and tangential velocity profiles at Station 6 corresponding to inlet condition IC6, as presented in Figure 11, are very close to the profiles given by Weber *et al.* at the same Station. If Weber *et al.*'s claims of numerical accuracy are to be believed, then this observation suggests that their comparatively poor results are a consequence of incorrectly specifying the turbulence profiles across the inlet plane. Indeed, further evidence that they have in fact committed such an error is given by their plot of the turbulence flux integrated over an entire cross section. Their plot shows a noticable rise in the turbulence flux in the region just upstream of the front stagnation point. This is also consistent with our results for the IC6 case, which corresponds to significantly higher turbulence levels in the approach flow than is experimentally observed. Final confirmation of the proposed source of error in Weber *et al.*'s results is given by examining their plot of the turbulence quantity $\sqrt{2k/3}$ at Station 4. With the exception of the integrated turbulence flux plot, this is the only such plot of turbulence quantities given by Weber *et al.*, and here again their results yield a profile similar to that obtained for the IC6 case in this work (see Figure 12).

The comments just made underline the fact that if turbulence models are to be correctly assessed for this class of flows, then great care in modelling upstream flow conditions must be exercised. Furthermore, the ongoing need for detailed and accurate measurements where sources of error are unambiguously quantified is highlighted. In particular, if the upstream

conditions are insufficiently mapped out with respect to both mean and turbulence quantities, then there exists considerable uncertainty as to whether a reliable turbulence model assessment can be made.

In the light of the totality of results presented thus far, it is useful to speculate at this point as to the inadequacy of the $k-\epsilon$ model for the modelling of this flow setup. With reference to the results at Station 4 and 6 in Figure 12, we assert that the key ingredient in the Std $k-\epsilon$ model's failure to predict the observed forward flow region in the IRZ is its overprediction of turbulence activity in the upstream region of the computed recirculation zone.

The assertion just made should be contrasted with a commonly cited reason for the inadequacy of the $k-\epsilon$ model, namely the built–in assumption of an isotropic eddy–viscosity. As the results to be presented for Model R1 in the next section will show, this possibility can be excluded as the primary reason for the shortcoming in the modelling at this level.

Model R1

Sensitivity to outlet conditions

For model R1, computations using the Quick scheme on $L = 1.5m/182 \times 24$ grid, $L = 2m/232 \times 24$ grid and $L = 3m/334 \times 24$ grid using inlet condition IC1 were initially undertaken to assess the effect of the outlet plane location on the computed results. The grid densities used are those shown earlier to give grid–independent results for the Std model.

An immediate assessment could not be made because model R1 failed to converge clearly to a final steady state using typical underrelaxation factors for the iterative scheme, and sample tests using a greater degree of underrelaxation did not clearly control oscillations in the solution process. However, by the monitoring various locations throughout the computational domain, it was established that the unsteadiness in the solution arrays with iteration count was locally confined. The main region of unsteadiness occured near the upstream portion of bounding shear layer within the IRZ, corresponding approximately to the axial interval between Stations 4 and 6. Interestingly, this is the very region where a time–dependent instability called the precessing vortex core is sometimes observed in the recirculating zone of swirl burners [27].

A schematic of the approximate region and nature of the observed unsteadiness is given in Figure 13 in terms of the mean streamlines. Initially, a small annular recirculation zone is observed in the front portion of the IRZ. With increasing iteration count the annular zone diminishes in size and moves in the direction indicated by the arrow. Before the eye of the zone can reach axial Station 6, no trace of the reciculation zone remains, while at the same time a new annular zone begins to again emerge in the front portion of the IRZ. Elsewhere the locations of the mean streamlines do not change significantly with iteration count.

The local nature of the oscillations allows an assessment of the effect of the outlet plane location on the computed results to be made without first undertaking a time integration of the governing equations. Here the steady profiles at Stations 8, 9 and 10 were compared, and no differences to graphical accuracy between the $L = 2m$ and $L = 3m$ results could be detected, while the $L = 1.5m$ results were only very slightly different (typically less than about 2% of full scale). From these observations we conclude that the $L = 2m$ geometry will yield solutions which are independent of the exit plane location, and this is used in subsequent model R1 computations.

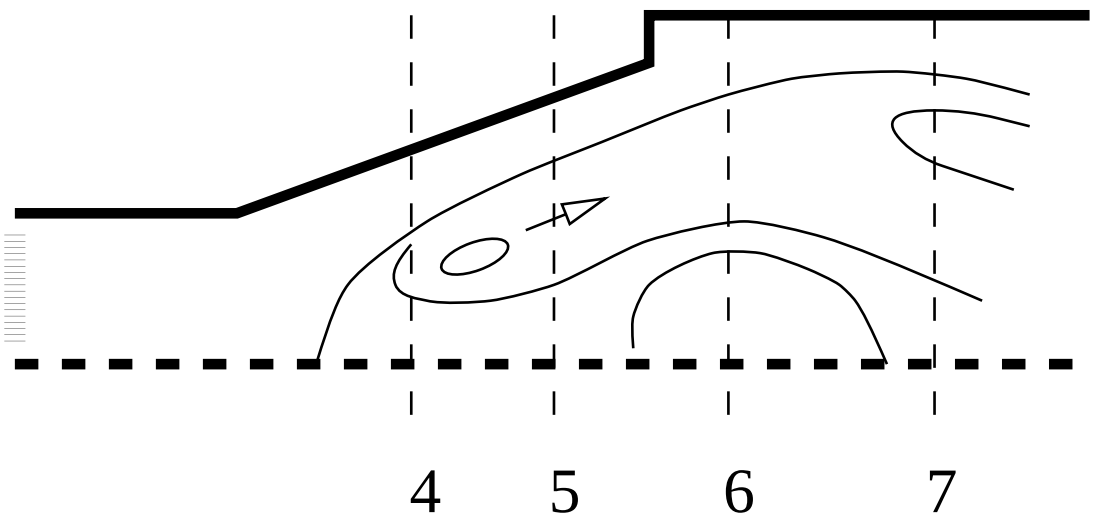

Figure 13: Schematic of region of unsteadiness for Model R1.

Time integration

To establish if the iterative unsteadiness was indicative of an underlying time dependence in the mean flow, a time integration of the governing equations was undertaken. As initial conditions a previously obtained quasi–steady solution is used. A fully implicit first order in time scheme is used, and a number of internal iterations are performed to ensure a spatially converged solution at each timestep. A range of timesteps are used to investigate whether the localised oscillations can be controlled, rather than to obtain a timestep–independent true transient plot of flow features.

In Figure 14, the time evolution of axial velocity at two points within the region of interest is shown. The latter correspond to locations in the computational domain where the oscillations were largest (see Figure 13). By using small timesteps, as illustrated, the oscillations in the iterative process can be completely controlled, and an unambiguously steady state solution is judged to have finally emerged (*i.e.* when local oscillations are everywhere less than 1%) some time after initial transients have decayed. Although not shown here, timesteps of $\Delta t = 0.01, 0.1, 1, 10$ and 100 were also used, and for $\Delta t > 0.1s$ oscillations did not decay in the transient plots.

Comparison with experiment

For model R1, a steady state solution is obtained by time integration for $9.25s$ using $\Delta t = 5 \times 10^{-4} s$, as described above. Inlet condition IC1 only is used for the model R1 computations.

In Figure 15, the model R1 mean axial velocity profiles at Stations 4, 5, 6, and 7 are shown. (Profiles at Stations 2 and 3 are similar to the Std model results and have been omitted.) In all respects the model R1 axial velocity profiles are dramatically improved over the Std model results, and closely mimic the experimental profiles. The shape and size of the peak, and the extent of flow near the symmetry axis are all more accurately predicted. The model R1 results shown in Figure 15 are clearly superior to both the $k-\epsilon$ model and more complex ASM

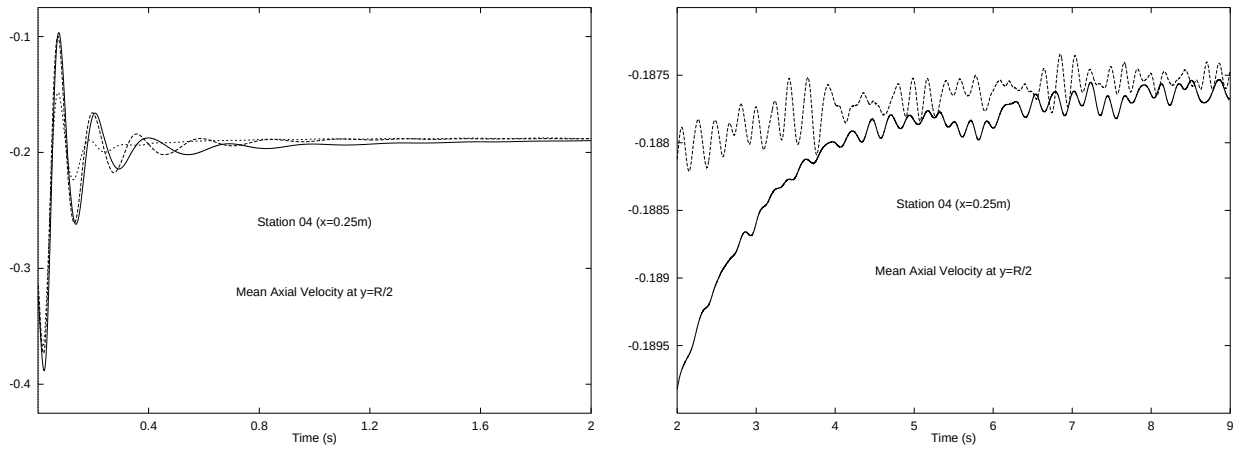

(a) Time evolution of Axial velocity at Stn 4 & $y = R/2$

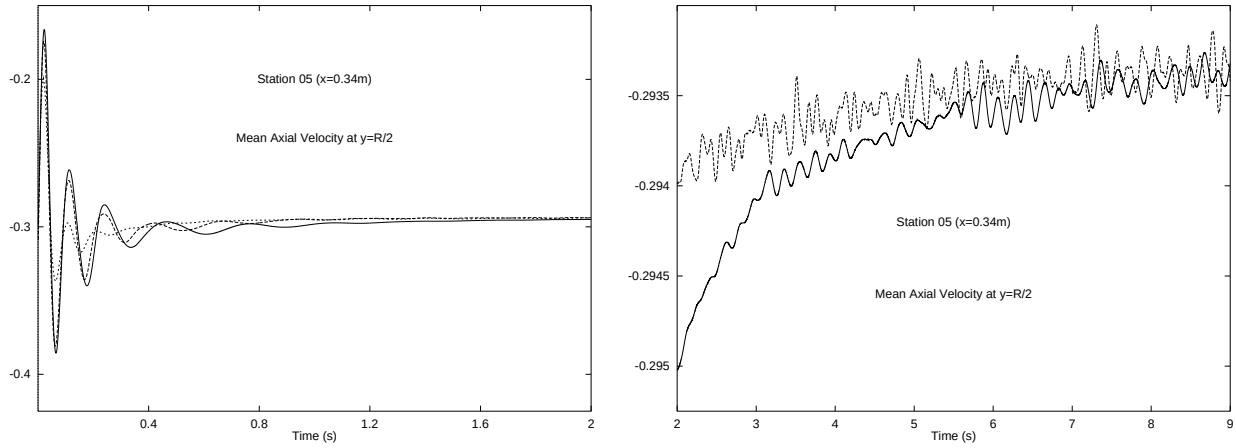

(a) Time evolution of Axial velocity at Stn 5 & $y = R/2$

Figure 14: R1 model/Quick/232 $\times$ 24 grid/$L = 2m$ mean axial velocity time histories at Stations 4 & 5 and $y = R/2$, using timesteps of $\Delta t = 5 \times 10^{-4} s$ (—), $\Delta t = 1 \times 10^{-3} s$ (– –), and $\Delta t = 5 \times 10^{-3} s$ (- - -).

results given by Benim. Furthermore, the profiles shown are equal or better than Weber *et al.*'s corresponding DSM results. The weak forward flow near the axis at Station 6, for example, was not captured in the corresponding DSM profile, and no forward flow region or multi–celled structure of the IRZ was evident in the mean streamlines, in contrast to mean streamlines to be presented shortly.

In Figure 16, mean tangential velocity and $\sqrt{2k/3}$ turbulence profiles at Stations 4, 5 and 6 are compared with experiment. The mean tangential velocity profiles at Stations 2 and 3 are in good agreement with the measurements and have again been omitted. The model R1 mean tangential velocity profiles are in general noticably improved, in particular at Stations 5 and 6.

The turbulence profiles presented in Figure 16 bring into sharp focus some important issues with regards to both the modelling and the flow physics.

Firstly, we note that the model R1 turbulence levels are, along with the mean velocity profiles, in good agreement with the measured distributions within the IRZ. The predicted model Std levels, by comparison, are far too high at these stations. These observations suggest that turbulence activity within the IRZ must be correctly modelled if mean velocity profiles in good agreement with experiment are to be obtained. The observations just made support our earlier

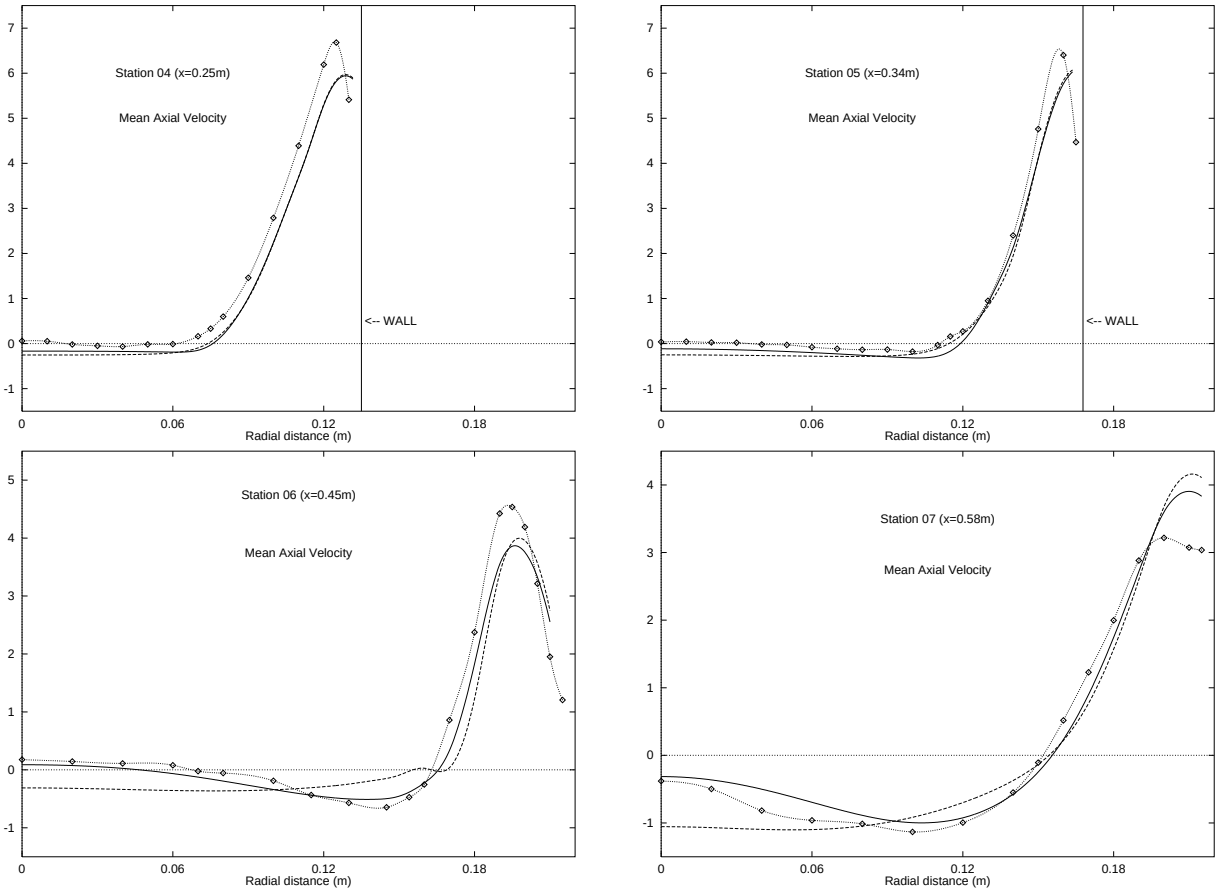

Figure 15: Comparison of Quick/232×24 grid/$L = 2m$ mean axial velocity profiles at Stations 4, 5, 6 & 7 for Model R1 (—) & Model R2 (– –) using IC1 inlet conditions, with Expt (– $\diamond$ –).

assertion that the key ingredient in the Std $k-\epsilon$ model's failure to predict the observed forward flow region in the IRZ is its overprediction of turbulence activity in the upstream region of the computed recirculation zone.

Secondly, we can ask to what extent can the results presented thus far, in particular the relative success of model R1, inform us as to the physics of the forward flow region of this highly confined vortex breakdown flow? In answering this question, we return again to Figure 16, and note that the anisotropy in the measured mean squared stresses within the IRZ is in fact not pronounced, and could be accounted for by an estimated 15% experimental error. Rather, the differences between the mean square axial and tangential velocity correlations at the plotted stations are clearly evident only in the bounding shear layer and in the vicinity of the wall. With this observation in mind, and given that the evidence presented thus far has suggested that the correct description of turbulence activity within the IRZ is the essential element in correctly predicting the mean flow within this zone, it comes as less of a surprise that an eddy–viscosity model that does not in any way account for the effects of normal stress anisotropy is actually capable of correctly capturing the forward flow region of the breakdown zone.

At this point it is useful to comment on whether there are any reasons why we could *a priori* expect only small differences in the mean square stress profiles within the IRZ. In this regard it is of interest to recall the work of Hogg & Leschziner [16], who argue that while the mechanisms governing the highly sensitive interaction between the mean swirl and turbulence energy are

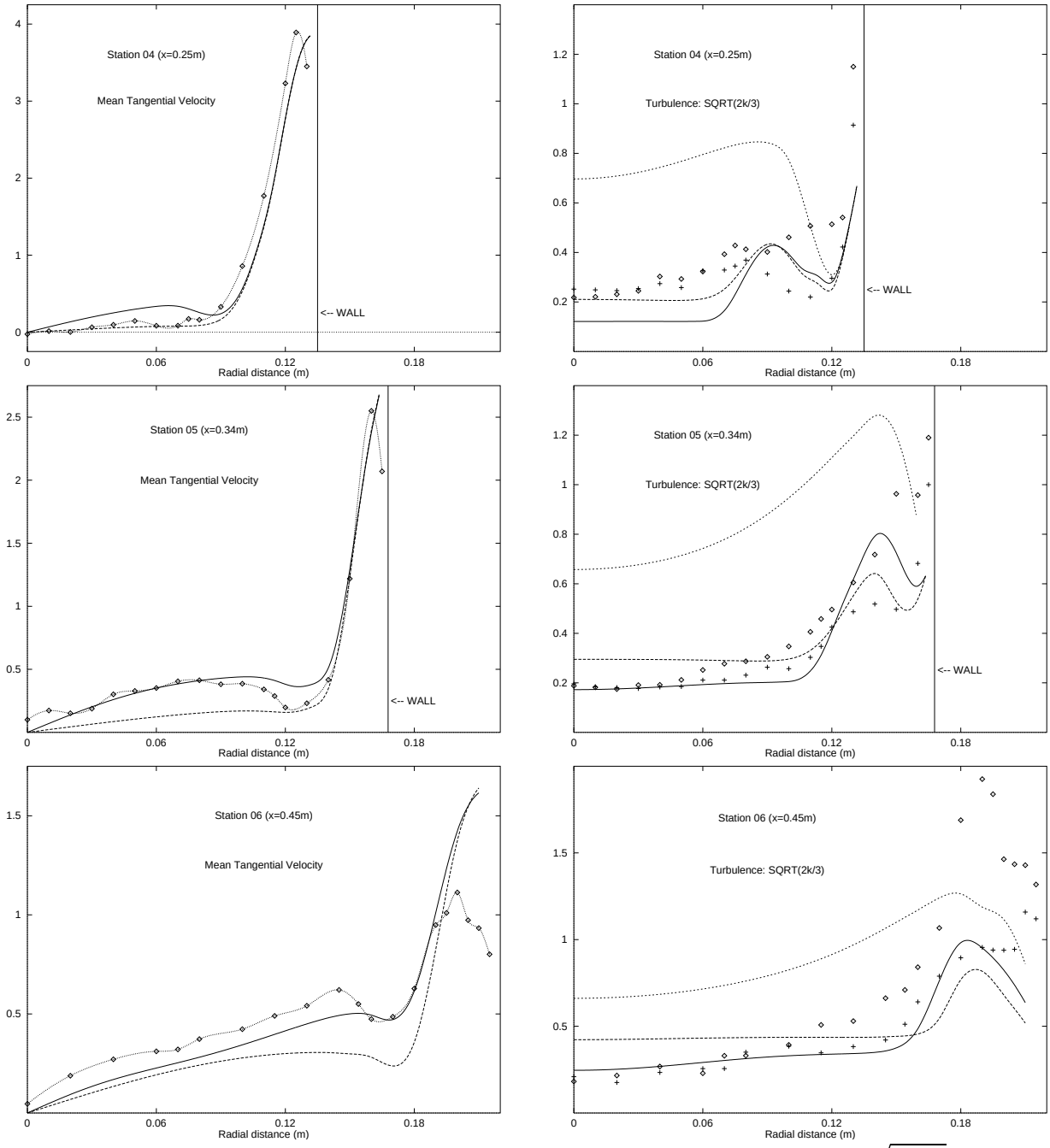

(a) Mean tangential velocity (b) Turbulence $\sqrt{2k/3}$

Figure 16: Comparison of Quick/232×24 grid/$L = 2m$ profiles at Stations 4, 5, & 6 using IC1 inlet conditions: (a) Mean tangential velocity for Model R1 (—) & Model R2 (– –) *c.f.* Expt ($-\diamond-$); (b) Turbulence $\sqrt{2k/3}$ for Model R1 (—), Model R2 (– –), & Model Std ($\cdots$) *c.f.* Expt (u' $\diamond$, w' $+$)

complex, they are essentially rooted in uneven swirl–related contributions to the production terms of the normal and shear stresses. They note that the latter involve products of the primary and secondary constituents of the rotational strain ($\partial W/\partial r - W/r$) and different stresses, this selective weighting tending to raise the level of normal stress anisotropy and materially modifying the shear stress field.

With the previous comments in mind, we recall that the present setup is highly confined, and

the upstream flow conditions are close to solid–body rotation. Thus, in the approach flow the rotational shear strain is almost identically zero, and cannot be responsible for generating significant turbulence levels. Furthermore, the axisymmetry condition implies that the flow within the IRZ must of necessity be close to solid–body rotation near the axis, thereby ensuring that any observed normal stress anisotropy in the vicinity of the axis is *not* due to local production via the rotational strain. In view of these comments it is hardly surprising that Hogg & Leschziner's DSM model calculations showed only minor departures from normal stress isotropy near the axis, although they themselves were disconcerted by the results, and supposed that the pressure–strain modelling (a weak element of the modelling at this level of closure), rather than the second moment closure's exact representation of stress production, was primarily responsible for the control of the stress levels. (Their nearly isotropic computed normal stresses, incidentally, were in fair agreement with those measured.)

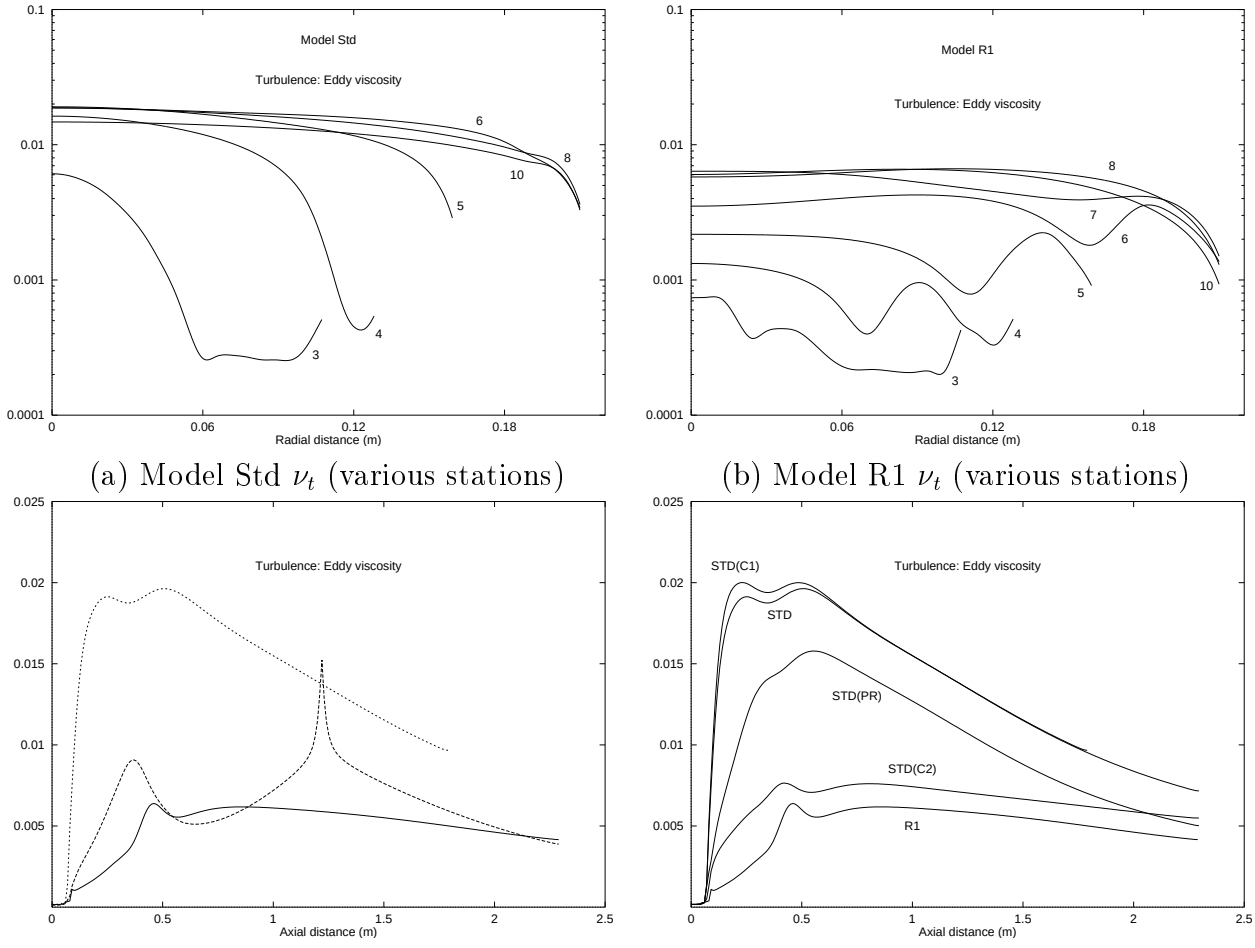

(a) Model Std ν_t (various stations)

(b) Model R1 ν_t (various stations)

(c) Centreline ν_t (various models)

(d) Centreline ν_t (various models)

Figure 17: Eddy viscosity profiles: (a) Model Std profiles at different Stations; (b) Model R1 profiles at different Stations. (c) Centreline profiles for Model R1 (—), Model R2 (– –) and Model Std ($\cdots$); (d) Centreline profiles for Model Std, Std(C1), Std(C2) and Std(Pr) (for Key see Table 6.)

In Figures 17(a) and 17(b) the predicted eddy viscosity profiles for models Std and R1 are given. It is interesting to note that at a given axial Station, both models yield approximately flat eddy viscosity profiles (*i.e.* $\nu_t \approx [Const.]$) on a cross sectional plane within the IRZ, especially near the symmetry line. On examination of the centreline eddy viscosity profiles in Figure 17(c), we

observe that for the Std model, the predicted eddy viscosity within the recirculation zone quickly rises to an approximately constant value immediately downstream of the front stagnation point. For the centreline eddy viscosity profile predicted by model R1, the increase just downstream of the front stagnation point is more gradual, and the maximum value is comparitively less by a factor of about 2.8. We note that an eddy viscosity which is constant across the flow (either with or without downstream variation) is reminiscent of self–preserving behaviour in turbulent jets and wakes, or flow in the outer part of a self–preserving turbulent boundary layer ([28] Ch 4 and 5).

Table 6: Std models with modified constants used in this study

Model	ν_t	σ_k	σ_ϵ	C_μ	$C_{\epsilon 1}$	$C_{\epsilon 2}$	R
Std	Eqn (6)	1.0	1.3	0.09	1.44	1.92	0
Std(C1)	Eqn (6)	1.0	1.3	0.085	1.42	1.92	0
Std(C2)	Eqn (6)	1.0	1.3	0.09	1.44	1.68	0
Std(Pr)	Eqn (6)	0.7179	0.7179	0.09	1.44	1.92	0
R1	Eqn (6)	0.7179	0.7179	0.085	1.42	1.68	0

The main reason for improved predictions obtained via model R1 appear to be due to the lower eddy viscosity values returned by the model, particularly in the forward region of the recirculating zone. It is of interest to investigate which model R1 modifications to the values of the model Std constants are responsible for this reduction. At this point we therefore performed a systematic study using the Quick/232×24 grid/$L = 2m$ computational model. Solutions were obtained with variants of the Std model where model constants were individually modified to the model R1 values, as shown in Table 6. A comparison of the centreline eddy viscosity profiles obtained from this study is shown in Figure 17(d). The results indicate that modifying the model constant $C_{\epsilon 2}$ from 1.92 to 1.68 leads to the greatest reduction in the eddy viscosity predicted by model Std. Setting the turbulent Prandtl numbers in model Std to $\sigma_k = \sigma_\epsilon = 0.7179$ also reduces the predicted eddy viscosity levels to a significant but lesser extent. The latter observation highlights, once again, that transport terms in the turbulence modelling are of importance to the overall prediction within the IRZ, as asserted earlier. It is also interesting to note that only model R1 shows a multi–celled IRZ flow structure in the mean streamlines. Given the relatively small differences in the centreline ν_t profiles predicted by models Std(C2) and R1 shown in Figure 17(d), the results suggest that the recirculating zone flow structure is sensitive to relatively small changes in the predicted eddy viscosity. This observation again supports our previous assertion that the turbulence levels within the IRZ significantly affect the recirculating zone flow structure.

To summarise our observations on the eddy viscosity results, we can say that to a first approximation, the Std model predicts that $\nu_t \approx [Const.]$ everywhere within the IRZ, while the model R1 results suggest that $\nu_t \approx \nu_t(x)$ within the recirculating zone. Given the relative success of model R1, these observations suggest that a very simple turbulence model, in the spirit of analyses for self–preserving flows, where the eddy viscosity is specified algebraically via $\nu_t = \nu_t(x)$ only, would have some likelihood of adequately capturing the complex multi–cellular mean flow features within the IRZ.

Finally, to summarise the totality of results presented in this section, we suggest that although in this highly confined solid–body flow the IRZ exhibits a complex multi–cellular flow structure, the primary underlying physics is arguably simpler than authors such as Hogg & Leschziner

have supposed. The observed normal stress isotropy near the symmetry axis suggests that eddy–viscosity turbulence models may be able to be used to predict the flow, although the very small contribution of the rotational shear to the modelled turbulence production apparently necessitates that a different set of constants for the $k-\epsilon$ model is needed, as demonstrated here. We have also found that a turbulence model which returns an approximately constant eddy viscosity across the flow within the IRZ leads to mean profiles which mimic the experimental data in the forward flow region of the recirculating zone. We note, however, that predictions appear to be relatively sensitive to small changes in the predicted eddy viscosity within the IRZ.

These findings must be qualified because, for example, we are basing our conclusions on results for a flow setup which is not characterised by high or highly anisotropic turbulence levels in the approach flow. For such cases, the possibly large or anisotropic enhancement of turbulence levels within the IRZ may necessitate the use of higher order modelling.

Sensitivity to wall conditions

Before leaving our discussion of the model R1 results, it is of interest to investigate to what extent the model R1 predictions depend on the wall boundary conditions. As a simple test, we replaced the log–law conditions by slip conditions for the axial and tangential velocities.

In general, the standard wall function treatment returns acceptable wall values for the mean axial and tangential velocities at the upstream stations, as can be seen in Figures 15 and 16, but tends to progressively overpredict the axial velocity wall values at stations further downstream. On the other hand, the use of slip conditions for the axial and tangential velocities does not attempt to capture the physics of the wall boundary layer. Interestingly, this simplification in the wall modelling leads to predicted wall values which are only about 5 to 15% higher at the upstream stations. This additional overprediction of wall values does not lead to significant differences in the upstream profiles.

Further downstream, the wall value of the mean axial velocity is seriously overpredicted by either boundary condition, as illustrated by a presentation of axial velocity profiles at Stations 8 and 9 in Figure 18(a). The computed wall values are more than twice those measured, and agreement is comparitively worse (by about 20 to 30%) when the slip boundary condition is used. We note that in the slip case, the increased wall value is accompanied by a corresponding increase in flow reversal near the symmetry axis. The latter is expected, as the mass flow rate must be conserved across each cross section. The results suggest that if wall values closer to the measurements were returned, then a decreased reversal near the symmetry axis would be predicted, in closer agreement with experiment. These observations suggest that the profiles far downstream are largely determined by the wall boundary conditions rather than the bulk flow turbulence modelling. This assertion is indirectly supported by the DSM results of Weber *et al.*, who also used standard wall functions. Their downstream profiles are no better than those given here.

In Figure 18(b), the tangential velocity profiles at Stations 8 and 9 are shown. Agreement between the computed wall values and experiment is again comparitively worse when the slip boundary condition is used. While the model R1 profiles are in general a little low, they otherwise correctly mimic the measured behaviour quite well when either wall boundary condition is used. In particular, both the measurements and the model R1 computations predict a slight

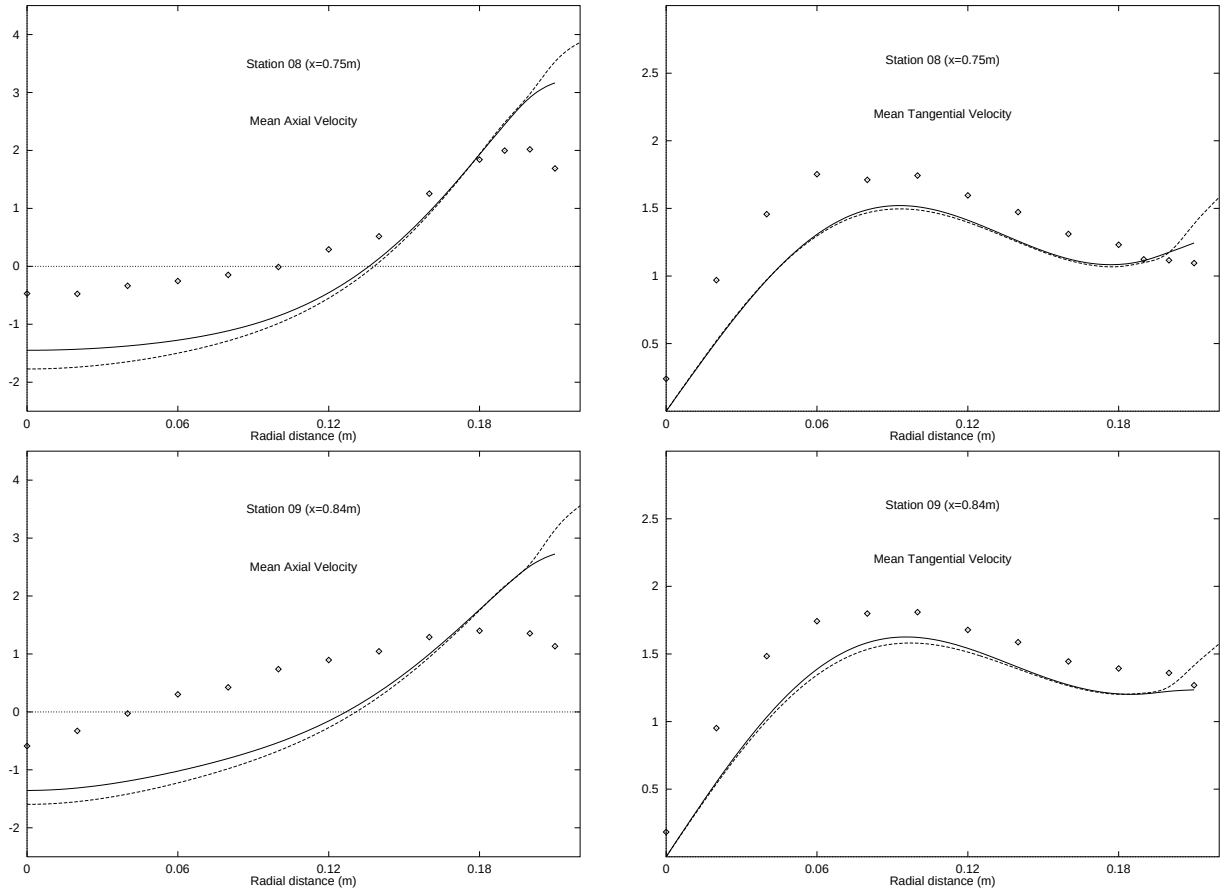

(a) Mean axial velocity (b) Mean tangential velocity

Figure 18: Comparison of Quick/232 × 24 grid/$L = 2m$/IC1 axial and tangential velocity profiles at Stns 8 & 9 with wall function (—) & slip (– –) wall boundary conditions, *c.f.* Expt ($\diamond$).

recovery in swirl velocity between Stations 8 and 9.

Model R2

Sensitivity to outlet conditions

For model R2, computations using the Quick scheme and inlet condition IC1 were performed on the $L = 1.5m/182 \times 24$ grid and $L = 2m/232 \times 24$ grid. For this model, steady state solutions were obtained without recourse to a time dependent calculation, and no differences to graphical accuracy between the $L = 1.5m$ and $L = 2m$ results could be seen. From these observations we conclude that the $L = 1.5m$ computational domain will yield solutions which are independent of the location of the exit plane. Results for model R2 presented here are obtained with the outlet located conservatively at $2m$ downstream from the quarl.

Comparison with experiment

The predicted model R2 axial velocity profiles are shown in Figure 15, while tangential velocity and turbulence profiles are presented in Figure 16. In general, the predictions for this model are much better than the Std model, but not as good as the model R1 results. Here again, a possible reason for the relative improvement over the Std model is that turbulence levels in the vicinity of the IRZ forward–flow region are significantly better captured, as indicated in Figure 16(b). The consequences for the predicted eddy viscosity are shown in Figure 17(c). We note from this Figure that while the downstream variation of ν_t predicted by model R2 is comparitively more complex, it lies generally somewhere between the model Std and R1 predictions.

Table 7: Quick/IC1 solution characteristics as a function of turbulence model.

Model	Grid	ψ_{min} (m^2/s)	ψ_{max} (m^2/s)	U_{min} (m/s)	U_{max} (m/s)	x_{front} (mm)	x_{back} (mm)	k_{max} (m^2/s^2)	$(\nu_t)_{max}$ (kg/ms)
Std	182×24	-.007225	.022776	-1.0777	5.9037	77.871	720.79	2.9176	.019627
R1	232×24	-.009515	.022759	-1.4532	5.9920	73.506	1471.2	1.5959	.006963
R2	232×24	-.011129	.022832	-1.9802	6.0242	72.920	1218.6	1.1073	.015468

In Table 7, key features of the solutions using models Std, R1 and R2 are compared. Of particular interest is the maximum eddy viscosity. For model R1, a 65% reduction in this quantity can be attributed to changing the values of the Std model constants to those predicted by the RNG theory. For model R2, the addition of further modelling features leads to a 21% reduction compared with the Std model. However, if we consider the peak eddy viscosity levels within the forward flow region of the IRZ only, then we observe that the differences between the model R1 and R2 predictions are not as great as the above percentages suggest. Referring again to Figure 17(c), we note that the local upstream maximum of centreline eddy viscosity for model R2 represents approximately a 55% reduction in this quantity compared with the model Std peak centreline value. Although the differences between the model R1 and R2 eddy viscosity profiles within the forward flow region of the IRZ are not great, these do result in significant changes in the mean profiles shown earlier in Figure 15 and 16. Here again, the upstream mean flow predictions prove to be rather sensitive to the predicted eddy viscosity levels, as we have already noted in the discussion of results illustrated in Figure 17(d).

A comparison of streamlines showing the predicted structure of the IRZ is given in Figure 19. Also included are the measured IRZ boundaries, taken from the results of Benim [1]. The latter are approximate only, in particular the location of the stagnation points in the forward flow region. In hindsight, the experimentalists should have included more transverse measurements across the forward flow region to accurately delineate this zone.

The inclusion of additional measurements across the downstream IRZ flow and terminus would have also allowed a more detailed study over the entire recirculating zone. We note, for example, that the axial location where the flow finally becomes unidirectional was not established. However, weak flow reversal on the axis was measured at Station 10, indicating that the location of the IRZ's downstream stagnation point is in the range $1095mm < x_{back} < 4m$. In Figure 19, the extreme downstream location of the streamline $\psi = 0$ for models R1 and R2 both lie in this range, whereas the recirculating zone predicted by model Std terminates far too early.

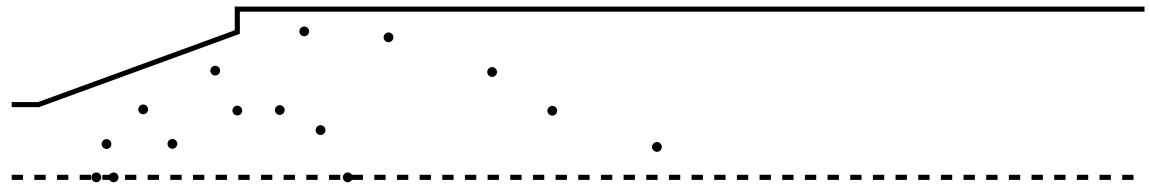

(a) Boundaries of the internal recirculation zone (approx.)

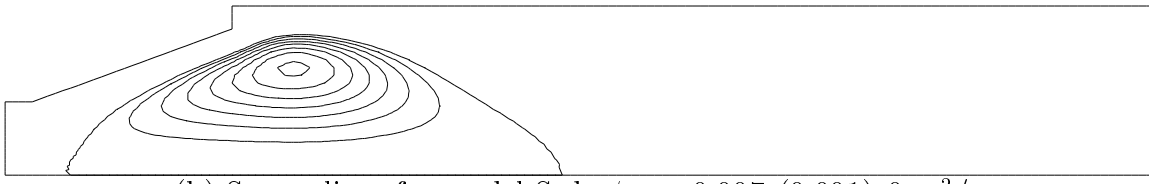

(b) Streamlines for model Std: $\psi = -0.007, (0.001), 0\ m^2/s$

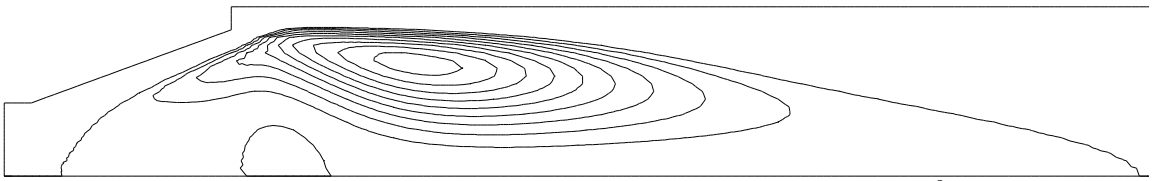

(c) Streamlines for model R1: $\psi = -0.009, (0.001), 0\ m^2/s$

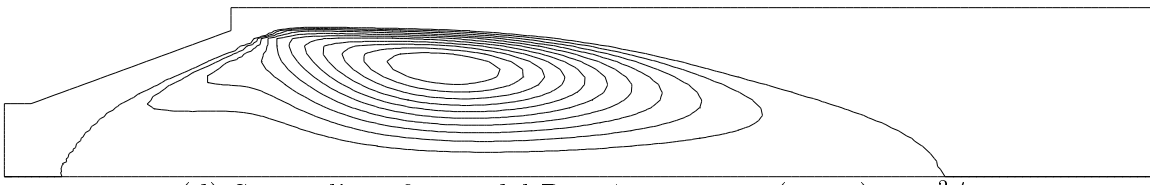

(d) Streamlines for model R2: $\psi = -0.010, (0.001), 0\ m^2/s$

Figure 19: Streamlines showing IRZ structure for models Std, R1 and R2.

It is interesting to note that for model R2, steady state solutions are obtained without recourse to a time dependent calculation. This indicates that model R2, like model Std, is less prone to iterative unsteadiness than model R1, even though all three models are essentially of the same level of complexity.

Conclusions

A computational study of turbulent flow in an axisymmetric quarl burner has been reported here. We find that a two–equation $k - \epsilon$ model, with modified constants predicted by RNG theory, captures the experimentally observed forward flow region of the turbulent inner recirculating zone. The strength of this finding is established via a detailed investigation of the effects of upstream and downstream conditions on the predictions, in addition to grid refinement and other tests to ensure that numerical error is not significant. This finding is in apparent contrast to previous studies.

Acknowledgement

Financial support for this work was provided in part by BHP research. Computing resources were supplied to the Centre in Statistical Science and Industrial Mathematics under Digital Equipment Agreement ERP No 2057.

References

[1] A. C. Benim. Finite element analysis of confined turbulent swirling flows. *Int. J. Num. Meth. Fluids*, 11:697–717, 1990.

[2] T. B. Benjamin. Theory of the vortex breakdown phenomenon. *J. Fluid Mech.*, 14:593–629, 1962.

[3] T. B. Benjamin. Significance of the vortex breakdown phenomenon. *J. Basic Eng.*, 87:518–524, 1965.

[4] T. B. Benjamin. Some developments in the theory of vortex breakdown. *J. Fluid Mech.*, 28:65–84, 1967.

[5] H. F. Boysan. Renormalization group theory based turbulence models and their applications to industrial problems. In *Engineering applications of computational fluid mechanics European Conference IMechE 1993–5*, pages 43–47. Institution of Mechanical Engineers, 1993.

[6] D. Choudhury. Introduction to the RNG method and turbulence modelling. Technical Report TM-107, Fluent, Inc., 1993.

[7] D. Choudhury. Fluent v4.3 validation problems. Technical Report TM-202, Fluent Inc., Lebanon, NH 03766, 1995.

[8] M. Dong and D. G. Lilley. Inlet velocity profile effects on turbulent swirling flow predictions. *Journal of Propulsion and Power*, 10(2):155–160, 1994.

[9] P. A. Durbin. On the k–3 stagnation point anomaly. *Int. J. Heat and Fluid Flow*, 17:89–90, 1996.

[10] J. H. Faler and S. Leibovich. An experimental map of the internal structure of a vortex breakdown. *J. Fluid Mech.*, 86:313–335, 1978.

[11] C. A. J. Fletcher. *Computational techniques for fluid dynamics*, volume I of *Springer series in computational physics*. Springer-Verlag, 2nd edition, 1991.

[12] S. Fu, P. G. Huang, B. E. Launder, and M. A. Leschziner. A comparison of algebraic and differential second-moment closures for axisymmetric turbulent shear flows with and without swirl. *J. Fluids Eng.*, 110:216–221, 1988.

[13] A. Hagiwara, S. Borz, and R. Weber. Theoretical and experimental studies on isothermal expanding swirling flows with application to swirl burner design - results of the NFA 2-1 investigations. Technical Report Doc. F 259/a/3, IFRF, 1986.

[14] M. G. Hall. The structure of concentrated vortex cores. *Progress in Aeronautical Sciences*, 7:53–110, 1966.

[15] M. G. Hall. Vortex breakdown. *Annu. Rev. Fluid Mech.*, 4:195–217, 1972.

[16] S. Hogg and M. A. Leschziner. Computation of highly swirling confined flow with a Reynolds-stress turbulence model. *AIAA J.*, 27:57–63, 1989.

[17] W. P. Jones and A. Pascau. Calculation of confined swirling flows with a second moment closure. *J. Fluids Eng.*, 111:248–255, 1989.

[18] N. A. Kelson, D. L. S. McElwain, and J. S. Truelove. Evaluation of $k - \epsilon$ and RNG turbulence models for confined swirling flow. In R. L. May and A. K. Easton, editors, *Computational Techniques and Applications: CTAC95*, pages 417–424. World Scientific, Singapore, 1996.

[19] M. A. Leschziner and W. Rodi. Calculation of annular and twin parrallel jets using various discretization schemes and turbulence-model variations. *J. Fluids Eng.*, 103:352–360, 1981.

[20] M. A. Leschziner and W. Rodi. Computation of strongly swirling axisymmetric free jets. *AIAA J.*, 22:1742–1747, 1984.

[21] M. Nikjooy and H. C. Mongia. A second–order modeling study of confined swirling flow. *Int. J. Heat and Fluid Flow*, 12:12–19, 1991.

[22] S. V. Patankar. *Numerical heat transfer and fluid flow.* Hemisphere, 1980.

[23] R. Peyret and T. D. Taylor. *Computational methods for fluid flow.* Springer-Verlag, 1983.

[24] M. A. R. Sharif and Y. K. E. Wong. Evaluation of the performance of three turbulence closure models in the prediction of confined swirling flows. *Computers and Fluids*, 24(1):81–100, 1995.

[25] D. G. Sloan, P. J. Smith, and L. D. Smoot. Modelling of swirl in turbulent flow systems. *Prog. Energy Combust. Sci.*, 12:163–250, 1986.

[26] R. E. Spall, T. B. Gatski, and R. L. Ash. The structure and dynamics of bubble-type vortex breakdown. *Proc. R. Soc. Lond. A*, 429:613–637, 1990.

[27] N. Syred, T. O'Doherty, and D. Froud. The interaction of the precessing vortex core and reverse flow zone in the exhaust of a swirl burner. *Proceedings of the Institute of Mechanical Engineers Part A: Journal of Power and Energy*, 208:27–36, 1994.

[28] H. Tennekes and J. L. Lumley. *A first course in turbulence.* MIT Press, Cambridge, Mass., 1972.

[29] J. S. Truelove. The use and abuse of mathematical models of flames and combustion. In *The Australian symp. on combustion incl. 3rd Aust. flame days*, Newcastle, NSW, 1993. Keynote lecture 2.

[30] J. P. van Doormaal and G. D. Raithby. Enhancements of the SIMPLE method for predicting incompressible fluid flow. *Numer. Heat Transfer*, 7:147–163, 1984.

[31] B. T. Vu and F. C. Gouldin. Flow measurements in a model swirl combustor. *AIAA Journal*, 20:642–651, 1982.

[32] A. Wanik and U. Schnell. Some remarks on the Piso and Simple algorithms for steady turbulent flow problems. *Computers Fluids*, 17:555–570, 1989.

[33] R. Weber, B. M. Visser, and F. Boysan. Assessment of turbulence modeling for engineering prediction of swirling vortices in the near burner zone. *Int. J. Heat and Fluid Flow*, 11:225–235, 1990.

[34] V. Yakhot and S. A. Orszag. Renormalization group analysis of turbulence. I. basic theory. *J. Scientific Comput.*, 1:3–51, 1986.

[35] V. Yakhot, S. A. Orszag, S. Thangam, T. B. Gatski, and C. G. Speziale. Development of turbulence models for shear flows by a double expansion technique. *Phys. Fluids A*, 4:1510–1520, 1992.

[36] V. Yakhot and L. M. Smith. The Renormalization group, the ϵ-expansion and derivation of turbulence models. *J. Scientific Comput.*, 7:35–61, 1992.